

Vesicularity, bubble formation and noble gas fractionation during MORB degassing.

Geoffroy J. Aubry, Nicolas Sator and Bertrand Guillot

Laboratoire de Physique Théorique de la Matière Condensée, Université Pierre et Marie Curie (Paris 6),

UMR CNRS 7600, case courrier 121, 4 place jussieu, 75252 Paris cedex 05, France.

ABSTRACT

The objective of this study is to use molecular dynamics simulation (MD) to evaluate the vesicularity and noble gas fractionation, and to shed light on bubble formation during MORB degassing. A previous simulation study (Guillot and Sator (2011) GCA 75, 1829-1857) has shown that the solubility of CO_2 in basaltic melts increases steadily with the pressure and deviates significantly from Henry's law at high pressures (e.g. ~ 9.5 wt% CO_2 at 50 kbar as compared with ~ 2.5 wt% from Henry's law). From the CO_2 solubility curve and the equations of state of the two coexisting phases (silicate melt and supercritical CO_2), deduced from the MD simulation, we have evaluated the evolution of the vesicularity of a MORB melt at depth as function of its initial CO_2 contents. An excellent agreement is obtained between calculations and data on MORB samples collected at oceanic ridges. Moreover, by implementing the test particle method (Guillot and Sator (2012) GCA 80, 51-69), the solubility of noble gases in the two coexisting phases (supercritical CO_2 and CO_2 -saturated melt), the partitioning and the fractionation of noble gases between melt and vesicles have been evaluated as function of the pressure. We show that the melt/ CO_2 partition coefficients of noble gases increase significantly with the pressure whereas the large distribution of the $^4He/^{40}Ar^*$ ratio reported in the literature is explained if the magma experiences a suite of vesiculation and vesicle loss during ascent. By applying a pressure drop to a volatile bearing melt, the MD simulation reveals the main steps of bubble formation and noble gas transfer at the nanometric scale. A key result is that the transfer of noble gases is found to be driven by CO_2 bubble nucleation, a finding which suggests that the diffusivity difference between He and Ar in the degassing melt has virtually no effect on the $^4He/^{40}Ar^*$ ratio measured in the vesicles.

Keywords: computer simulations, MORB, supercritical CO_2 , noble gases, vesicularity, bubble formation, partition coefficient

34 1. Introduction

35 Noble gases are important tracers to understand the evolution and the degassing of the Earth's
36 mantle through time (Allègre et al., 1983; Harper and Jacobsen, 1996; Pepin, 2006). The elemental
37 fractionation of noble gases and their isotopes recorded in oceanic basalts (MORBs and OIBs), if
38 properly deciphered, may give information on the source region and on the details of noble gas
39 transport up to the surface. For instance the difference in $^3\text{He}/^4\text{He}$ ratios between MORBs and OIBs is
40 at the basis of the canonical model in isotope geochemistry (Porcelli and Wasserburg, 1995; Graham,
41 2002) describing the lower mantle as undegassed (high $^3\text{He}/^4\text{He}$ ratio) and the upper mantle as
42 degassed (low $^3\text{He}/^4\text{He}$ ratio). But this model is in conflict with other data (e.g. the *He* paradox,
43 Anderson, 1998) and is periodically revisited (Meibom et al., 2003; Parman et al., 2005; Albarède,
44 2008; Gonnermann and Mukhopadhyay, 2009). On the other hand, MORB and OIB glasses show a
45 large distribution of the $^4\text{He}/^{40}\text{Ar}^*$ ratio (~ 1 -1000, where Ar^* is corrected for air contamination) which
46 is interpreted as the signature of different degassing scenarios. Thus a low $^4\text{He}/^{40}\text{Ar}^*$ ratio (~ 1) is
47 explained by a closed system degassing where a CO_2 -saturated basaltic melt (CO_2 is the main volatile
48 component in oceanic basalts before H_2O , noble gases being present as traces) vesiculates by CO_2
49 exsolution and ascends with very little vesicle loss, up to the seafloor where volatiles are released (e.g.
50 Sarda and Graham, 1990). In contrast, a high $^4\text{He}/^{40}\text{Ar}^*$ ratio can be accounted for either by a Rayleigh
51 distillation process (Burnard, 1999; Moreira and Sarda, 2000; Colin et al., 2011), by a suite of
52 vesiculation and vesicle loss during magma ascent (Sarda and Graham, 1990; Sarda and Moreira,
53 2002) or by a kinetic disequilibrium occurring just before eruption (Aubaud et al., 2004). However
54 CO_2 has a very low solubility in basaltic melts at pressure corresponding to the seafloor (~ 0.5 ppmw at
55 one bar, Dixon (1997)) and therefore an overwhelming majority of erupting lavas are strongly
56 degassed and have lost their pristine volatile contents.

57 Remarkable exceptions are *popping rocks* (Hekinian et al., 1973) characterized by high CO_2
58 contents (~ 1 wt% CO_2 in the sample $2\pi D43$, Sarda and Graham (1990), Javoy and Pineau (1991)) a
59 large vesicularity (>10 % in volume), and a $^4\text{He}/^{40}\text{Ar}^*$ ratio (~ 1.5 in $2\pi D43$) compatible with the

60 expected K/U ratio of the mantle (Allègre et al., 1987). These tholeiitic basalts likely have experienced
61 a CO_2 exsolution in the oceanic mantle and for this reason are considered as probing the source region
62 (Sarda and Graham, 1990; Javoy and Pineau, 1991). Nonetheless, a pending question is to know if
63 magmas even richer in CO_2 do exist and may exsolve a CO_2 -rich fluid at greater depth in the mantle.
64 In this context, it is noteworthy that evidences of explosive eruptions at ocean spreading centers are
65 well documented (Hekinian et al., 2000; Eissen et al., 2003; Pineau et al., 2004; Sohn et al., 2008;
66 Clague et al., 2009; Shaw et al., 2010; Helo et al., 2011). The presence of extended volcanoclastic
67 deposits at great water depth ($\sim 4,000$ m) suggests that this explosive volcanism with magma disruption
68 could be driven by CO_2 -rich melts (Sohn et al., 2008; Helo et al., 2011). More generally, there are
69 growing evidences of the existence of CO_2 -rich magmas in the upper mantle. Thus, seismological and
70 magnetotelluric data suggest that incipient melting may begin at depths of 150-300 km in the upper
71 mantle (Evans et al., 2005; Bologna et al., 2011). Experimental petrology data shows that deep melting
72 can occur with carbonate-silicate assemblages leading to carbonatitic liquids at very low melt fraction
73 (Eggler, 1976; Dalton and Pressnall, 1998; Dasgupta and Hirschmann, 2006; Zeng et al., 2010;
74 Rooney et al., 2012). So, the electrical anomalies of the oceanic asthenosphere could be explained by
75 ~ 0.1 % volume fraction of carbonatite melts circulating in the silicate mantle (Gaillard et al., 2008).
76 This melt fraction corresponds on average to ~ 300 ppmw CO_2 stored in the asthenosphere, a value
77 compatible with various estimates of the CO_2 contents in the source region of MORB (Marty and
78 Tolstikhin, 1998; Saal et al., 2002; Cartigny et al., 2008). Furthermore these carbonatites can
79 metasomatize the surrounding silicate matrix and lead to melt mixing during their ascent (Dixon et al.,
80 2008).

81 When an upwelling volatile-bearing melt reaches the CO_2 saturation limit, the excess of CO_2 is
82 exsolved by forming bubbles or vesicles. The noble gases initially present in the melt as traces (less
83 than a ppmw, Moreira et al., 1998) fractionate between melt and CO_2 bubbles in a proportion which
84 depends both on the vesicularity and on their respective solubility (or partition coefficient) in the two
85 coexisting phases (Jambon et al., 1986). When a tholeiitic basalt vesiculates at shallow depth under the
86 seafloor (e.g. a few kilometers), a simple way to estimate the noble gas partitioning is to assume that

87 the fluid filling the vesicles is an ideal gas and that the solubility of noble gases in the basaltic melt is
88 that measured at laboratory at low pressures (Henry's law). Because noble gas solubilities in basaltic
89 melts are very low ($S_{He-Xe} \sim 10^{-5} - 10^{-8} \text{ bar}^{-1}$, where S is the inverse of Henry's constant, Jambon et al.
90 (1986)), noble gases partition preferentially into the CO_2 bubbles, the heavier the noble gas the higher
91 the fraction. This is the common view of closed-system noble gas degassing.

92 A different situation is encountered if the CO_2 saturation limit is reached at great depth in the mantle
93 (e.g. in the oceanic asthenosphere). The vesicles are filled with a very dense supercritical CO_2 fluid
94 which limits the transfer of noble gases from the melt. A theoretical approach of this mechanism has
95 been proposed by Sarda and Guillot (2005) and Guillot and Sarda (2006) by using a hard sphere model
96 to describe the silicate melt, the fluid CO_2 , and the incorporation of noble gases in the two coexisting
97 phases. An important conclusion of this study is that the noble gas fractionation between melt and
98 vesicles at high pressures deviates significantly from a simple evaluation based on noble gas solubility
99 data at low pressures (Henry's law) and for which the deviation from ideality of the CO_2 fluid is
100 neglected. Although this model is useful for theoretical guidance, there is a need for improvement. For
101 instance, the solubility of CO_2 in silicate melts and especially in basalts is well documented at low
102 pressures where Henry's law holds (Stolper and Holloway, 1988; Dixon et al., 1995; Jendrzejewsky et
103 al., 1997; Botcharnikov et al., 2005) but is poorly known at high pressures above ~ 20 kbar (Pan et al.,
104 1991; Brooker et al., 2001). Recently Guillot and Sator (2011) have evaluated by molecular dynamics
105 simulation (MD) the pressure evolution of the CO_2 solubility in silicate liquids of various composition.
106 In basaltic melts the calculated CO_2 solubility increases steadily above 20 kbar (where $X_{CO_2} \sim 1.6 \text{ wt\%}$)
107 and reaches $\sim 20 \text{ wt\%}$ at 80 kbar, a value much higher than the one estimated from Henry's law
108 ($X_{CO_2}^H \sim 0.5 \text{ ppmw per bar}$, see Dixon et al. (1995)). These simulation results are in agreement with a
109 few solubility data in melts of basaltic composition obtained from high-pressure partial melting
110 experiments of silicate-carbonate assemblages (Hammouda, 2003; Thomsen and Schmidt, 2008).

111 Our objective is to evaluate by atomistic simulation, the pressure dependence of noble gas
112 partitioning between a CO_2 -saturated MORB melt and a coexisting CO_2 phase (closed system

113 degassing), as also as the noble gas fractionation in melt and in vesicles during MORB degassing. For
 114 that we have implemented the *test particle method* (TPM) to calculate the chemical potential of a trace
 115 element (e.g. a noble gas) into a melt or a high density fluid (CO_2) modeled by MD simulation. This
 116 method has been recently used to evaluate the solubility of noble gases in high-pressure silicate liquids
 117 (Guillot and Sator, 2012). The theoretical framework and the simulation details are explained in
 118 section 2, and the results are presented and discussed in section 3. In section 4, the kinetics of bubble
 119 formation and noble gas transfer is investigated by devising a numerical experiment where a pressure
 120 drop is applied to a volatile bearing MORB melt. The implications of such a decompression
 121 experiment are discussed.

122 2. Method of calculation

123 2.1 Noble gas partitioning in a vesiculated MORB melt.

124 When a volatile bearing MORB melt is ascending under an oceanic ridge, it starts to degas when the
 125 ambient pressure becomes lower than the saturation pressure of the major volatile component present
 126 in the melt (Sparks, 1978; Bottinga and Javoy, 1990). In a MORB melt where CO_2 is the major
 127 volatile component and noble gases are traces, the latter ones redistribute between CO_2 bubbles and
 128 bulk melt. At given temperature (T) and pressure (P) conditions, the equality of the chemical
 129 potentials of a noble gas i in the vesiculated melt and in the CO_2 bubbles leads to the following
 130 relationship,

$$131 \rho_m^i / \rho_v^i = e^{-(\mu_m^{i,ex} - \mu_v^{i,ex}) / k_B T} = \gamma_m^i / \gamma_v^i \quad (1)$$

132 where k_B is the Boltzmann constant, T the temperature, ρ_m^i and ρ_v^i are the number densities (number
 133 of atoms per unit volume) of the noble gas i in the melt and in the vesicles (CO_2 bubbles), respectively,
 134 and where $\mu_m^{i,ex}$ and $\mu_v^{i,ex}$ are the excess chemical potentials of the noble gas in the corresponding
 135 phases (notice that the ideal parts of the chemical potentials cancel out because they are identical in the
 136 two phases). The quantity $\gamma_{m,v}^i = e^{-\mu_{m,v}^{i,ex} / k_B T}$ is named the solubility parameter in the corresponding

137 phase (m or v). By introducing V_m the volume of melt and V_v the total volume of vesicles the Eq.(1)
 138 leads to the following equality,

$$139 \quad \frac{N_m^i}{N_v^i} = \left(\frac{V_m}{V_v}\right) \cdot \left(\frac{\gamma_m^i}{\gamma_v^i}\right) \quad (2)$$

140 where N_m^i is the number of noble gas atom in the melt and N_v^i the one in the vesicles.

141 For a closed system degassing, N_m^i and N_v^i are related by the following mass conservation law,

$$142 \quad N_0^i = N_m^i + N_v^i \quad (3)$$

143 where N_0^i is the number of noble gas atom i in the CO_2 -bearing MORB melt before vesiculation.

144 Following the derivation of Guillot and Sarda (2006), the final step consists to introduce Eq.(3) into

145 Eq.(2) and to make use of the definition of the vesicularity, $V^* = V_v / (V_v + V_m)$. After some elementary

146 algebra the numbers of noble gas atom i in the melt and in the vesicles are equal to,

$$147 \quad N_m^i = N_0^i \cdot \left(\frac{\gamma_m^i}{\gamma_v^i}\right) \cdot (1 - V^*) / \left[V^* + \left(\frac{\gamma_m^i}{\gamma_v^i}\right) \cdot (1 - V^*)\right] \quad (4)$$

$$148 \quad N_v^i = N_0^i \cdot V^* / \left[V^* + \left(\frac{\gamma_m^i}{\gamma_v^i}\right) \cdot (1 - V^*)\right]. \quad (5)$$

149 The above expressions are exact at equilibrium (for any thermodynamic condition) and they replace

150 the ones obtained by Jambon et al. (1986) which are valid only at very low pressure when the CO_2

151 fluid filling the vesicles can be considered as ideal (in this case $\gamma_v^i = 1$) and γ_m^i can be approximated

152 by the solubility constant S^i in using Henry's law,

$$153 \quad \gamma_m^i = \rho_m k_B T S^i \quad (6)$$

154 where ρ_m is the numerical density of the melt. However, the simplicity of expressions (4) and (5) is

155 somewhat misleading because to evaluate N_m^i and N_v^i at given (T,P) conditions, the vesicularity of the

156 degassing melt must be known and the solubility parameters γ_m^i and γ_v^i evaluated in the coexisting

157 phases at these very thermodynamic conditions.

158 To estimate the evolution of the vesicularity with the thermodynamic conditions one needs to know
 159 the pressure (and temperature) behaviour of the CO_2 solubility in the MORB melt. As a matter of fact,
 160 in using the equality of the chemical potentials of CO_2 in the melt and in the vesicles as also as the
 161 mass conservation law for the CO_2 molecules, it can be shown that the vesicularity, V^* , fulfils the
 162 following relationship,

$$163 \quad \frac{V^*}{1-V^*} = \left(\frac{n_m}{n_v} \right) \cdot \left[\frac{\frac{(1-W)}{W}}{\frac{(1-W_0)}{W_0}} - 1 \right] \quad (7)$$

164 where n_m and n_v are the densities of the CO_2 -saturated silicate melt and of the CO_2 fluid filling the
 165 vesicles at (T,P) of interest, W is the solubility of CO_2 (in g_{CO_2}/g_{melt}) in the silicate at (T,P)
 166 conditions during magma ascent, and W_0 is the CO_2 content in the melt before degassing ($W < W_0$). If
 167 exsolution only occurs when a degree of super saturation in CO_2 is reached (i.e. when magma ascent is
 168 so rapid that chemical equilibrium cannot be achieved) then the term "-1" on the right hand side of
 169 Eq.(7) may be replaced by "- α " where the super saturation ratio, $\alpha = X_w^{CO_2}(P, T)/W(P, T)$, expresses
 170 the ratio of the weight fraction of CO_2 molecules actually in the melt to the one expected at saturation.
 171 In the following $\alpha (\geq 1)$ will be used as an adjustable parameter.

172 2.2 Calculation of noble gas solubility parameters.

173 As expressed by Eqs.(4) and (5), in a closed system degassing, the partitioning of a noble gas i
 174 between melt and vesicles depends on the vesicularity, V^* , and on the ratio of the solubility
 175 parameters, γ_m^i/γ_v^i . In a seminal work, Widom (1963) has shown that the solubility parameter, γ_s^i , of a
 176 solute i at infinite dilution in a solvent s can be written under the following form,

$$177 \quad \gamma_s^i = e^{-\mu_s^{i,ex}/k_B T} = \langle e^{-\psi/k_B T} \rangle_{N_s} \quad (8)$$

178 where $\psi = (U_{N_s+1} - U_{N_s})$ is the potential energy difference between a mixture composed of N_s
 179 solvent molecules plus the solute particle (e.g. a noble gas atom) and the pure solvent. In the case
 180 where the potential energy is pairwise additive (i.e. $U_{N_s+1} = \sum_{i < j = 1, N_s+1} u_{ij}$ where i and j are two

181 particles and u_{ij} the pair interaction energy), ψ is nothing but the solute-solvent interaction energy
 182 ($\psi = \sum_{j \in N_s} u_{1j}$ where u_{1j} is the interaction energy between the solute particle 1 and the solvent
 183 particle j). A key feature of Eq.(8) is that the canonical average $\langle e^{-\psi/k_B T} \rangle_{N_s}$ is taken over the
 184 configurations of the pure solvent, the solute particle acting as a ghost (or test) particle. In practice, the
 185 solute (i.e. the noble gas atom) is inserted at random in the solvent configurations generated by MD
 186 simulation and the Boltzmann factor, $\langle e^{-\psi/k_B T} \rangle_{N_s}$, is evaluated by averaging over all insertion
 187 events. However, when the solvent density is high, the noble gas atom randomly inserted has a high
 188 probability to overlap a solvent molecule. The consequence is a strongly repulsive solute-solvent
 189 interaction energy ($\frac{\psi}{k_B T} \gg 1$) leading to a vanishingly small contribution of this event to the average
 190 ($e^{-\psi/k_B T} \ll 1$). What is needed for practical use of this method is a numerical recipe for detecting
 191 quickly undesirable positions of the inserted noble gas atom and for locating cavities that can
 192 accommodate it, cavities that appear and disappear at the mercy of the solvent density fluctuations. We
 193 have implemented the sampling method of Deitrick et al. (1989) which makes the evaluation of the
 194 solubility parameter by the test particle method (TPM) very effective. For a detailed description of the
 195 method and a discussion of the statistical uncertainties, the reader is referred to the paper by Guillot
 196 and Sator (2012) where the solubility of noble gases in silicate melts was evaluated in this framework.

197 To evaluate the noble gas solubility parameters γ_m^i and γ_v^i by the TPM one needs to generate by MD
 198 simulation a suite of atomic configurations which are representative of the CO_2 -bearing basaltic melt
 199 and of the CO_2 fluid assumed to coexist with each other at a given state point (T,P). The accuracy of
 200 the calculation relies on the force field used to describe the interactions between the atoms of the
 201 phases under consideration. Six different kinds of interaction are involved: CO_2 - CO_2 interaction,
 202 silicate-silicate interaction, CO_2 -silicate interaction, noble gas- CO_2 interaction, noble gas-silicate
 203 interaction and noble gas-noble gas interaction. Notice that noble gases are trace elements in the
 204 mantle (on average much less than a ppmw in MORBs) and therefore can be considered at infinite
 205 dilution both in the MORB melt and in the CO_2 bubbles. For silicate-silicate, CO_2 - CO_2 and CO_2 -
 206 silicate interactions we have used the pair potentials developed by Guillot and Sator (2007a,b; 2011) in

207 their MD studies of dry and CO_2 -bearing silicate melts of various composition (the corresponding
 208 potential parameters are listed in Table 1 of Guillot and Sator (2011) and are not reproduced here).
 209 When CO_2 is incorporated into the basaltic melt, a reactive force field accounts for the chemical
 210 reactivity between the oxygens of the silicate and CO_2 molecules,



212 the equilibrium concentrations in CO_2 and carbonate ions (CO_3^{2-}) depending at once on the melt
 213 composition, the investigated thermodynamic conditions (T,P) and the total CO_2 content. In the case of
 214 a MORB composition, the CO_2 solubility curve has been investigated by Guillot and Sator (2011) at
 215 isothermal conditions (between 1673 and 2273K) up to 150 kbar. We have used these simulation data
 216 as benchmarks for preparing our CO_2 +MORB compositions.

217 To evaluate the interaction energy between noble gases and the elements of the silicate melt, we
 218 have implemented the atom-atom Lennard-Jones potentials recently developed by Guillot and Sator
 219 (2012), a force field which successfully reproduces the solubility data of noble gases in liquid silicates.
 220 As for the interactions between CO_2 and the noble gases we have developed specifically for the
 221 present study a force field based on the Lennard-Jones pair potential. The derivation of the potential
 222 parameters is presented in Appendix and their values are listed in Table A1.

223 **2.3 Simulation details**

224 Two series of MD runs were performed, one corresponding to a CO_2 -saturated basaltic melt at various
 225 thermodynamic conditions, and the other one corresponding to the CO_2 phase assumed to be in
 226 coexistence with the melt. The composition of the simulated MORB (in wt%: 50.59 SiO_2 , 1.5 TiO_2 ,
 227 15.11 Al_2O_3 , 1.15 Fe_2O_3 , 8.39 FeO , 7.77 MgO , 11.87 CaO , 2.94 Na_2O and 0.13 K_2O) is the one of a
 228 sample (*TK21B*) of the mid-atlantic ridge. This composition has been investigated by Guillot and Sator
 229 (2011) to determine the CO_2 solubility curve as function of T and P. So the CO_2 contents at saturation
 230 used in the present study are those determined by these authors at T=1873K and P=10, 20, 30, 50, 80,
 231 and 100 kbar. With regard to the CO_2 -saturated MORB melt, the simulation cell is composed of 1,000

232 ions (or 5,000 ions, to estimate system size effects) plus the necessary number of CO_2 molecules to
233 reach CO_2 saturation at the investigated state point (the simulation conditions are summarized in Table
234 1). The coexisting CO_2 phase is simulated independently from the CO_2 -saturated melt and is composed
235 of 500 (or 2,500) molecules.

236 The MD calculations were performed with the DL_Poly 2.0 code (Smith and Forrester, 1996). The
237 equations of motion for ions and CO_2 molecules were solved with a time step of 10^{-15} s. The simulation
238 box is cubic with periodic boundary conditions and the long range coulombic interactions are
239 accounted for by an Ewald sum. For the two systems (the CO_2 bearing melt and the CO_2 phase) the
240 calculations were first performed in the isothermal isobaric ensemble (N,P,T) for equilibration and
241 next were carried on in the microcanonical ensemble (N,V,E) for generating production runs. The
242 latter ones were 10^{-8} s long (i.e. 10^7 MD steps) for small system sizes (N=1,000 ions for MORB and
243 500 molecules for fluid CO_2), and 10^{-9} s long for large system sizes (5,000 ions and 2500 molecules,
244 respectively). The statistical uncertainties on each investigated state point are about 1% for density,
245 pressure and temperature. At each state point under consideration, atomic configurations were stored
246 every $2 \cdot 10^{-12}$ s (i.e. 2,000 MD steps) to be sampled afterwards by the TPM (this time interval is chosen
247 so as the displacement of atoms between two successive recording is of the order of an atomic
248 diameter, i.e. $\sim 3A$).

249 As mentioned in section 2.2, the TPM was optimized in implementing the sampling procedure of
250 Deitrick et al. (1989). A description of this recipe is discussed in details in Guillot and Sator (2011)
251 and is not reproduced here. In short, the simulation box containing the atomic configurations to be
252 sampled is divided into small cubelets (e.g. $100 \times 100 \times 100$). A cubelet is marked as occupied if its
253 center is located within the repulsive core of a solvent atom. Thus, only insertions where the test
254 particle is addressed to an unoccupied cubelet contribute to the average $\langle e^{-\psi/k_B T} \rangle_{N_s}$. However, the
255 free volume accessible to the test particle (the volume fraction corresponding to unoccupied cubelets)
256 decreases drastically with the size of the test particle (the noble gas) to insert and with the density of
257 the solvent (the higher the density the smaller the free volume). For instance, the free volume

258 accessible to He in a MORB melt at 10 kbar is 19%, whereas it is equal to 12% for Ne, 1.3% for Ar
 259 and only 0.04% for Xe. At 50 kbar the free volume amounts to 11% for He, 5.5% for Ne, 0.2% for Ar
 260 and 0.002% for Xe. Thus, the occurrence to find at the mercy of density fluctuations, a cavity large
 261 enough to accommodate an Ar atom in a basaltic melt at 50 kbar is a rare event. This is why it is
 262 necessary to perform long MD runs with a system size large enough. Moreover, it is important that the
 263 number of cubelets mapping the simulation box is large enough to be certain that all cavities
 264 susceptible to accommodate the noble gas atom have been sampled.

265 With regard to the MD simulations, the parameters to be fixed are the system size and the length of
 266 the MD run. When these two parameters are fixed, the numerical uncertainties associated with the
 267 evaluation of the solubility parameters ($\gamma_{m,v}^i$) by the TPM increase drastically with the size of the
 268 noble gas to insert and with the density (i.e. with the pressure) of the solvent (for a discussion see
 269 Appendix A in Guillot and Sator, 2012). To estimate these uncertainties we have performed two
 270 independent series of MD calculations which approximately lead to the same computational cost. One
 271 series was performed with small system sizes (see Table 1) over a long simulation time (10 ns) and
 272 another series with larger system sizes but over a shorter simulation time (1ns). The results of these
 273 calculations are presented in Table 2. A fair agreement is found between the two series of calculations
 274 for He and Ne in the two phases (the deviation is less than 3 percent) and for Ar in CO_2 (except at 100
 275 kbar where $\Delta\gamma_v^{Ar}/\gamma_v^{Ar} \sim 14\%$). However the deviation becomes more significant for Ar in the MORB
 276 melt above 50 kbar (e.g. $\Delta\gamma_m^{Ar}/\gamma_m^{Ar} \sim 20\%$ at 50 kbar and $\sim 40\%$ at 100 kbar) and is quite large for Xe in
 277 MORB from 30 kbar ($\sim 300\%$ at 30 kbar). A drastic reduction of the uncertainties for Xe in MORB at
 278 high pressures would require to perform very long MD runs (~ 1000 ns) with a large number of atoms
 279 (10^5 - 10^6), a task which is too demanding for our numerical resources. Consequently values of γ_m^{Xe} for
 280 pressure above 30 kbar will be discarded in the following. In considering that the calculations
 281 performed with the two system sizes are independent from each other, the final values of γ_m^i and γ_v^i
 282 have been obtained simply by doing the arithmetic mean of the two series of calculations.

283

284 3. Results

285 3.1 Vesicularity of MORBs

286 Before discussing the fractionation of noble gases between melt and vesicles it is worthwhile to
 287 analyze the pressure evolution of the vesicularity of a degassing magma (closed system degassing). In
 288 Fig.1 is reported the pressure dependence of the vesicularity of an ascending magma, described by our
 289 simulated MORB melt, at isothermal condition (1873 K) and for different initial conditions of CO_2
 290 saturation at depth (with $P_{CO_2}^{sat} = 100, 80, 50, 30, 10, 5,$ and 1 kbar). The vesicularity, V^* , is evaluated
 291 from Eq.(7) in using for the pressure evolution of the CO_2 solubility (W) the one calculated by Guillot
 292 and Sator (2011), whereas the density (n_m) of the CO_2 bearing MORB melt and the density (n_v) of the
 293 coexisting CO_2 fluid are deduced from the present simulation study. By inspecting Fig.1, it appears
 294 that the growth rate of the vesicularity of an ascending magma is correlated with the CO_2 content of
 295 the source region (see in Fig.1 the evolution of the curvature of the vesicularity curve with increasing
 296 $P_{CO_2}^{sat}$). For instance, a MORB melt CO_2 -saturated at $P_{CO_2}^{sat} = 10$ kbar (d~30 km) will show a vesicularity
 297 of 10% in erupting at 5,500 m below sea level (m.b.s.l.) whereas the one of an ascending magma CO_2 -
 298 saturated at $P_{CO_2}^{sat} = 100$ kbar (i.e. d~300 km) will reach 10% at $P = 90$ kbar (d~270 km) and 50% at 15
 299 kbar (d~45 km). So, if it exists a source region very enriched in CO_2 in the oceanic mantle (from a
 300 carbonatitic origin, for instance), the magma issuing from this setting will become highly vesiculated
 301 at great depth. In that case the supercritical CO_2 fluid is characterized by a liquid-like density (e.g.
 302 $n_{CO_2} \sim 1.40$ g/cm³ at 30 kbar) and a degassing process at this depth is more related to a liquid-liquid
 303 immiscibility than to a gas bubble formation.

304 Actually, an overwhelming majority of MORB samples collected at oceanic ridges exhibit a weak
 305 or moderate vesicularity. In Fig.1 are reported vesicularity data obtained by Chavrit (2010) from the
 306 analysis of 65 MORB samples collected at the atlantic, pacific and indian ocean ridges and those of
 307 Hekinian et al. (2000) and Pineau et al. (2004) for MORB samples dredged on seamounts of the mid-
 308 atlantic ridge. These MORB samples were collected between ~1,000 and 5,000 m.b.s.l. (i.e. ~0.1-0.5
 309 kbar of hydrostatic pressure). If one assumes that the observed vesicularity is due to a closed system

310 degassing without loss of vesicles between the source region and the seafloor, then our calculations
 311 suggest than most of the MORB samples are issuing from a source region located at shallow depth
 312 ($P_{CO_2}^{sat} \leq 5$ kbar i.e. $d < 15$ km). Moreover, if exsolution only occurs when some degree of super
 313 saturation in CO_2 is reached (for illustration, the dotted curves shown in Fig.1 correspond to a degree
 314 of super saturation $\alpha=2$), our calculations indicate that the vesicularity observed at eruption will be
 315 significantly lowered if the source region of the CO_2 -saturated magma is located at shallow depth (for
 316 instance, if $P_{CO_2}^{sat}=1$ kbar, the vesicularity at 4,000 m.b.s.l. is three times smaller for a melt exhibiting a
 317 super saturation $\alpha=2$ than for a melt erupting at equilibrium). Incidentally, a super saturation in CO_2 is
 318 frequently reported in the bulk melt of MORB samples (Dixon et al., 1988; Jendrzejewski et al., 1997;
 319 Aubaud et al., 2004; Cartigny et al., 2008) and it seems to be higher when the vesicularity is low
 320 ($< 1\%$, see Chavrit, 2010).

321 In contrast, for CO_2 -rich magmas their high vesicularity at eruption is barely affected by a possible
 322 super saturation (see dotted curves in Fig.1 when $V^* \geq 10\%$). With regard to those rare MORB
 323 samples exhibiting a high vesicularity ($> 10\%$ in Fig.1), their source region is likely located at a depth
 324 between ~ 15 km and ~ 90 km (i.e. $P_{CO_2}^{sat} \sim 5-30$ kbar). For instance, the *2πD43 popping rock*, which is
 325 considered as an undegassed MORB sample, likely is issuing from a CO_2 -saturated magma located at
 326 ~ 36 km depth ($P_{CO_2}^{sat} \sim 12$ kbar, according to Fig.1). In the same way, the highly vesiculated samples
 327 ($V^* \geq 0.50$ in Fig.1) collected in the rift valley of the mid-atlantic ridge near $34^\circ N$ (Hekinian et al.,
 328 2000; Pineau et al., 2004), and which are associated with volcanoclastic deposits, could be issued from
 329 CO_2 -saturated magmas at $P_{CO_2}^{sat} \sim 20-28$ kbar (see Fig.1), a source region located about 60-90 km in the
 330 oceanic mantle. Moreover, according to our results, a magma saturated in CO_2 at 30 kbar reaches the
 331 fragmentation limit, $V^*=0.75$ (Sparks, 1978; Namiki and Manga, 2008), if it erupts at about 1,600
 332 m.b.s.l., precisely the depth at which volcanoclastic deposits are observed. Notice that to reach the
 333 fragmentation limit at a greater water depth (e.g. 4,000 m.b.s.l.) the magma must be saturated in CO_2
 334 at a much higher pressure (e.g. ~ 50 kbar or at 150 km in the upper mantle, according to Fig.1).

335 A more quantitative way to compare the vesicularity of MORB samples with that deduced from
336 simulation data is to represent the vesicularity measured (or evaluated) at a given hydrostatic pressure
337 as function of the total CO_2 content in the undegassed sample. Experimentally, the CO_2 content is
338 evaluated by summing the amount of CO_2 in the bulk melt, measured by step heating or by IR
339 spectroscopy, and that in the vesicles, measured by crushing or estimated from the vesicularity in
340 treating the CO_2 phase filling the vesicles as an ideal gas (Graham and Sarda, 1991; Javoy and Pineau,
341 1991; Hekinian et al., 2000; Pineau et al., 2004). However, the CO_2 content in the glass is generally
342 much smaller than the one in the vesicles, except for samples exhibiting a very low vesicularity
343 ($V^* \leq 10^{-3}$). In Fig.2 is reported the vesicularity as function of the total CO_2 content (in g_{CO_2}/g_{melt}) of
344 MORB samples collected at the Atlantic, Indian and Pacific ocean ridges at various water depth
345 (minimum and maximum water depths are indicated in the figure). These experimental data (Chavrit
346 (2010) and Pineau et al. (2004)) are compared with our calculations for a CO_2 -saturated magma
347 ascending under isothermal condition ($T=1873$ K) and erupting at 1,000 m.b.s.l. (upper dots) or at
348 5,000 m.b.s.l. (lower dots), these two depths enclosing approximately the range of depth encountered
349 at oceanic ridges. The agreement with experimental data is remarkable, especially if one emphasizes
350 that the vesicularity of MORBs is evaluated from glassy samples whereas the vesicularity of our
351 model is for a liquid sample erupting at 1873 K. It is commonly admitted (even if this is questionable)
352 that the vesicularity of a magma erupting on the seafloor is frozen in when the temperature of the melt
353 passes through the glass transition temperature ($T_g \sim 1000$ K, Ryan and Sammis (1981)). But if one
354 considers that the solubility of CO_2 at the pressure of eruption changes very little when the
355 temperature drops (Pan et al., 1991), and that the CO_2 phase filling the vesicles behaves as an ideal
356 gas, then the vesicularity at T_g will be smaller than the vesicularity of the high temperature liquid just
357 before eruption by a ratio equal to T_g/T (~ 0.53 for the simulated MORB at 1873 K). Nevertheless, this
358 estimation has to be taken with some caution as it likely overestimates the decrease of the vesicularity
359 during the quench. As a matter of fact, upon rapid cooling, the viscosity of a basalt can be sufficiently
360 high even above T_g to limit vesicle shrinkage (Gardner et al., 2000). However, the important point is
361 that a small decrease of the vesicularity is expected in going from the liquid to the glass, a feature

362 which can explain why the calculated vesicularity is systematically (but slightly) larger than the
 363 observed one in Fig.2. For instance, the *2πD43 popping rock* dredged at 3,770 m on the mid-atlantic
 364 ridge has a vesicularity of 17% and a CO_2 content evaluated around 0.85-1.24 wt% (Graham and
 365 Sarda, 1991; Javoy and Pineau, 1991; Cartigny et al., 2008; Chavrit, 2010) as compared with 20-28%
 366 for the vesicularity of our simulated melt at 1873 K bearing the same CO_2 content. It is noteworthy
 367 that the calculations presented in Fig.2 do not take into account a possible super saturation in CO_2 . We
 368 have emphasized earlier that the vesicularity of a melt erupting on the seafloor is significantly affected
 369 by super saturation only when the source region is very shallow (a few km in the oceanic crust). In this
 370 case the vesicularity of the super saturated melt can be much smaller than the one of a sample at
 371 equilibrium (this is illustrated in Fig.1 for a super saturation equal to 2). The very low vesicularity
 372 exhibited by MORB samples of the Pacific ridge (see the crosses in Fig.1 and 2) can then be explained
 373 in noting that their degree of super saturation is in the range 1.5-2.5 (Chavrit, 2010).

374 In conclusion, the large distribution of vesicularity which characterizes MORB samples can be
 375 described by a CO_2 degassing process initiated at various depths in the oceanic mantle. However, the
 376 vesicularity observed after eruption on the seafloor is only the evidence of the last vesiculation episode
 377 experienced by the ascending magma, an evidence which gives no information about the degassing
 378 history prior this episode (if any). But, as discussed in the following, complementary information
 379 about the degassing trajectory can be obtained from the inventory of noble gases.

380 **3.2 Partitioning and fractionation of noble gases.**

381 According to Eqs.(4) and (5), the partitioning of noble gases between melt and vesicles is controlled
 382 by γ_m^i and γ_v^i , the noble gas solubility parameters in the two coexisting phases. Values of these
 383 parameters evaluated by the TPM at isothermal condition (T=1873 K) are listed in Table 2 as function
 384 of the pressure. For a given noble gas (*He*, *Ne*, *Ar* or *Xe*) both solubility parameters, γ_m^i and γ_v^i ,
 385 decrease strongly when the pressure is increased, whereas at a given pressure, the heavier the noble
 386 gas the smaller the solubility parameters in the two coexisting phases ($\gamma^{He} > \gamma^{Ne} > \gamma^{Ar} > \gamma^{Xe}$). These
 387 trends are similar to those obtained by Guillot and Sator (2012) in their study of the solubility of noble

388 gases in dry silicate melts. According to Eq.(2) the ratio, γ_m^i/γ_v^i , is equal to ρ_m^i/ρ_v^i , where ρ_m^i is the
 389 number density of noble gas of species i in the CO_2 -saturated melt (i.e. the number of noble gas atoms
 390 in the melt per volume of melt) and ρ_v^i is the one in the CO_2 phase. This ratio is nothing but the noble
 391 gas partition coefficient which expresses the distribution of the noble gas (i) between the two phases.
 392 As shown in Fig.3, the noble gas partition coefficient increases with the pressure but tends to level off
 393 above 50 kbar. More precisely, between 0 and 50 kbar the partition coefficient for He increases by
 394 $\sim 400\%$, that for Ne by $\sim 500\%$ and that for Ar by $\sim 600\%$. This pressure effect implies that the transfer
 395 of a noble gas from the melt to the vesicles is hindered at depth (high P) by the high density of the CO_2
 396 phase filling the vesicles. So, to properly estimate the melt/ CO_2 partitioning of noble gases in a magma
 397 at depth, it is inaccurate to use the low pressure solubility of noble gases in the basaltic melt and to
 398 consider the CO_2 phase as an ideal gas (for which $\gamma_v^i=1$).

399 The inventory of noble gases in MORB samples is well documented (Graham, 2002). In the
 400 following our analysis will focus on 4He and ^{40}Ar for which a consistent set of data is available. Before
 401 to compare these data with the prediction of our model calculation, it is worthwhile to examine how
 402 He and Ar distribute between melt and vesicles for a closed system degassing. In Fig.4 is shown the
 403 evolution of He and Ar contents, as calculated from Eqs.(4) and (5), in melt and in vesicles as function
 404 of the vesicularity evaluated for an hydrostatic pressure equivalent to 3,000 m.b.s.l. (the average water
 405 depth at oceanic ridges). The He and Ar contents are normalized with their initial abundance in the
 406 undegassed melt. Various initial CO_2 contents are investigated (controlled by the parameter W_0 in
 407 Eq.(7)). They correspond to a CO_2 -saturation pressure, $P_{CO_2}^{sat}$, varying from 100 to 0.4 kbar (the value
 408 of $P_{CO_2}^{sat}$ is indicated in Fig.4). An attentive examination of Fig.4 shows that when the vesicularity is
 409 large (i.e. $V^* \geq 10\%$ or $P_{CO_2}^{sat} > 5$ kbar), more than 99% of Ar atoms and 90% of He atoms are in the
 410 vesicles at eruption, whereas for a 1% vesicularity, about 90% of Ar atoms are in the vesicles but only
 411 40% of He atoms. If outgassing starts at very shallow depth, for instance at 1,000 m below the seafloor
 412 (i.e. at $P_{CO_2}^{sat}=0.4$ kbar), the vesicularity becomes as small as 0.2% and yet 60% of Ar atoms are in the
 413 vesicles when 90% of He atoms are staying in the melt. These results are easily understandable if one

414 recalls that the melt/ CO_2 partition coefficient for He is much greater than for Ar (a factor of ~ 10 , see
 415 Fig.3). So, according to the vesicularity of the sample at eruption, the fractionation of noble gases (i.e.
 416 the ratio He/Ar) in melt and in vesicles will be different.

417 In order to compare in absolute value the noble gas contents measured in MORB samples with those
 418 calculated from Eqs.(4) and (5), we make the assumption that the concentration in ^{40}Ar and the
 419 $^4He/^{40}Ar$ ratio extracted from the $2\pi D43$ *popping rock* reflect best the noble gas composition of the
 420 source region for MORBs (~ 0.1 ppmw of ^{40}Ar after correction for atmospheric contamination, and
 421 $^4He/^{40}Ar \sim 1.5$, see Moreira et al. (1998), Moreira and Sarda (2000) and Raquin et al. (2008)). In Fig.5
 422 is presented the evolution of Ar content in vesicles (in $10^{-6} \text{ g}_{Ar}/\text{g}_{melt}$) as function of the vesicularity of
 423 the simulated MORB evaluated at 3,000 m.b.s.l., and in Fig.6 is presented the evolution of the
 424 $^4He/^{40}Ar$ ratio. Here again, several initial conditions in CO_2 content for the source region are
 425 considered (the corresponding CO_2 -saturation pressure evolving from 50 to 0.4 kbar). In both figures
 426 are shown literature data (black squares) compiled by Chavrit (2010) and obtained by crushing MORB
 427 samples (for this reason only noble gas contents in vesicles are reported). It is clear that a simple
 428 closed system degassing (see the red dots defining the curve with index V^1 in Figs.5 and 6) is unable
 429 to reproduce the literature data except those of the $2\pi D43$ *popping rock* which are well represented by
 430 a single stage of vesiculation starting at ~ 30 km depth ($P_{CO_2}^{sat} \sim 10$ kbar). For the other MORB samples,
 431 the Ar contents in vesicles are found to be much weaker (by one to three orders of magnitude) than
 432 those predicted by a one-stage vesiculation mechanism. Correlatively, the $^4He/^{40}Ar$ ratios observed in
 433 MORB samples are generally much higher than predicted.

434 These findings imply that either the initial noble gas contents of the MORB source vary from one
 435 sample to another, or the degassing trajectory is more complex than the one described by a simple
 436 closed system degassing. Although it cannot be excluded that for some settings the noble gas contents
 437 may vary significantly or be affected by diffusive fractionation during mantle melting (Burnard, 2004;
 438 Burnard et al., 2004; Yamamoto et al., 2009), it is generally accepted that the upper mantle is
 439 compositionally homogeneous with regard to noble gases, and because the latter ones are incompatible

440 elements (Brooker et al., 1998; Chamorro et al., 2002; Brooker et al., 2003; Heber et al., 2007), the
 441 melt composition in noble gases reflects that of the solid mantle. In contrast, the C contents of the
 442 upper mantle likely is more heterogeneous (Saal et al., 2002; Cartigny et al., 2008). Furthermore it
 443 may happen that during ascent the magma loses its CO_2 -rich bubbles (e.g. slow ascent in a tortuous
 444 conduit), with the noble gases dissolved into it. Next, after this resetting step, the ascending melt starts
 445 again to degas when the residual amount of CO_2 oversteps the saturation limit. If this stage of vesicle
 446 loss occurs when the vesicularity of the magma is significant (a few percent or more) then the residual
 447 melt is strongly depleted in noble gases as a large proportion of the latter ones have been taken away
 448 with the CO_2 bubbles (see Fig.4 for the respective proportion of noble gases in melt and in vesicles).
 449 According to Sarda and Moreira (2002), Sarda and Guillot (2005) and Guillot and Sarda (2006),
 450 several stages of vesiculation followed by vesicle loss can explain the low ^{40}Ar contents and the high
 451 $^4He/^{40}Ar$ ratio measured in many of MORB samples.

452 In Figs.5 and 6 are reported the Ar content and the $^4He/^{40}Ar$ ratio in vesicles of the simulated MORB
 453 after having experienced several stages of vesiculation with vesicle loss. In practice, after each stage of
 454 vesicle loss, the noble gas content, N_m^i (with $i = He$ or Ar), figuring in Eq.(4), is substituted to N_0^i in
 455 Eqs.(4) and (5) while V^* is set to 0. For illustration, in Figs.5 and 6 are shown 2-stage (marked V^2), 3-
 456 stage (marked V^3) and 4-stage (marked V^4) vesiculations. In the case of V^2 , three degassing paths are
 457 presented (see blue dots): ($P_1=20$; $P_2=19, 18, \dots, 0.4$), ($P_1=5$; $P_2=4, 3, \dots, 0.4$) and ($P_1=1$; $P_2=0.9, 0.8, \dots,$
 458 0.4). The first number P_1 corresponds to the CO_2 saturation pressure (in kbar) at which the first
 459 vesiculation stage occurs, and the second number P_2 is the saturation pressure of the second
 460 vesiculation stage in assuming that in between the two stages, the ascending MORB melt has
 461 experienced a total loss of vesicles. In looking at Fig.5, one notices that the higher the pressure
 462 threshold P_1 of the first vesiculation (i.e. the deeper in the oceanic mantle the first degassing episode),
 463 the lower the Ar contents in vesicles of a MORB sample of a given vesicularity at eruption (e.g. for
 464 $V^*=1\%$ i.e. for $P_2=0.8$ kbar, the Ar content is equal to ~ 0.04 ppmw if $P_1=1$ kbar, ~ 0.0035 ppmw if
 465 $P_1=5$ kbar and ~ 0.0006 ppmw if $P_1=20$ kbar). As shown in Fig.5, it is clear that a 2-stage vesiculation
 466 process may account of a significant part of the literature data (compare the squares with the blue

467 dots). However, 3-stage and 4-stage vesiculations (or higher order) may be necessary to describe
 468 highly *Ar*-depleted samples ($<10^{-4}$ ppmw): two examples are given for illustration, \mathbf{V}^3 ($\mathbf{P}_1=20$; $\mathbf{P}_2= 3$;
 469 $\mathbf{P}_3=2, 1, \dots, 0.4$ see green dots) and \mathbf{V}^4 ($\mathbf{P}_1=20$; $\mathbf{P}_2= 3$; $\mathbf{P}_3= 1$; $\mathbf{P}_4= 0.9, \dots, 0.4$ see cyan dots). Incidentally,
 470 one notices that most of the measured vesicularities are below $\sim 5\%$, a value which suggests that most
 471 of MORB samples have experienced a last vesiculation episode not as deep as ~ 10 km in the mantle
 472 (or $P_{CO_2}^{sat} < 3$ kbar).

473 With regard to the ${}^4He/{}^{40}Ar$ ratio presented in Fig.6, similar conclusions are obtained (compare
 474 squares with dots in the figure). Thus in introducing a 2-stage vesiculation the ${}^4He/{}^{40}Ar$ ratio lies
 475 between 1 and 10, whereas higher values (~ 10 -100) are reached with 3- or 4-stage vesiculations.
 476 Nevertheless, the highest values of the ${}^4He/{}^{40}Ar$ ratio (in the range 100-1000) and the lowest *Ar*
 477 contents ($<10^{-4}$ ppmw) measured in MORB could originate from a Rayleigh distillation process
 478 (Moreira and Sarda, 2000; Burnard, 2001) where CO_2 bubbles are extracted from the melt as soon as
 479 they are formed (e.g. in a shallow magma chamber). But other mechanisms have been proposed to
 480 explain high values of the ${}^4He/{}^{40}Ar$ ratio as, for instance, a fractional crystallization-assimilation-
 481 degassing in a shallow magma chamber (Marty and Zimmermann, 1999) or a kinetic fractionation
 482 controlled by diffusion during incomplete degassing (Aubaud et al., 2004; Paonita and Martelli, 2006,
 483 2007). The cornerstone of this latter mechanism is that the larger diffusivity of *He* atoms into the
 484 MORB melt with respect to that of *Ar* and CO_2 may enrich in *He* atoms incipient CO_2 bubbles, a
 485 kinetic disequilibrium which can be frozen in at eruption if the ascent rate is sufficiently high. We
 486 show in the next section that this hypothesis can be tested by MD simulation.

487 **4. Kinetics of noble gas transfer during bubble formation**

488 In the course of a MD simulation it is possible to reproduce a degassing process in applying a
 489 pressure drop to a volatile-saturated melt. For instance, in starting from a well equilibrated CO_2
 490 bearing melt at 1873K and 50 kbar (the CO_2 content is ~ 9.5 wt%) and in applying a sudden pressure
 491 drop from 50 to 5 kbar, a 3D visualization of the simulation box shows the growth of a CO_2
 492 nanobubble fully developed after about a few ns of running time (see Fig.7). The vesicularity of the

493 MORB sample after the pressure drop is that expected from the thermodynamic relationship (see
494 Eq.(7) and Fig.1), i.e. about 30 % in the present case. Correspondingly the bulk melt around the CO_2
495 bubble has a CO_2 content of ~ 0.3 wt%, a value in agreement with the solubility of CO_2 at these
496 thermodynamic conditions (in Fig.7, the initial state is a melt made of 5,000 ions, ~ 176 carbonate ions
497 and ~ 99 CO_2 molecules, whereas the final state is a melt composed of 5,000 ions, ~ 2 carbonate ions
498 and ~ 6 CO_2 molecules and a bubble formed by ~ 267 CO_2 molecules). We have repeated the above
499 degassing experiment for other thermodynamic conditions (e.g. 100 \rightarrow 50 kbar, 100 \rightarrow 10 kbar, and
500 30 \rightarrow 3 kbar) and the final state is characterized by a single CO_2 bubble whose the size agrees with the
501 vesicularity estimated by thermodynamics. But, because of the small system size investigated (a few
502 thousand particles), only a few nucleation loci are observed initially in the simulation box (see Fig.7),
503 and hence it is not possible to investigate the nucleation rate quantitatively (very large system sizes are
504 then required). In practice, to render more effective bubble nucleation it is important to deal with a
505 high initial CO_2 content, i.e. to prepare the initial state at a high enough pressure (e.g. 100, 50 or 30
506 kbar), and to apply a large decompression rate (here the pressure drop is applied quasi instantaneously
507 over one MD step, i.e. 10^{-15} s, a more detailed analysis of bubble nucleation by changing the
508 decompression rate is beyond the scope of this article). But this is immaterial with regard to our
509 primary objective which is to quantify how fast is the transfer of noble gases from the melt to a
510 growing CO_2 bubble.

511 A small number (~ 10) of *Ar* or *He* atoms is incorporated into a CO_2 -saturated MORB melt at given
512 (T,P) conditions, and after a period of equilibration (~ 1 ns) the system is suddenly decompressed (e.g.
513 from 100 \rightarrow 10 kbar). It may happen that the number of noble gas atoms incorporated into the melt is
514 high enough for the melt to be supersaturated in noble gases (this is the case for Ar atoms but not for
515 He atoms in the pressure range investigated, for a discussion on noble gas solubility in silicate melts
516 see Guillot and Sator (2012)). However there is no evidence of noble gas atom clustering in the
517 simulated melt before decompression, likely because the nucleation rate for such an event is so low
518 that the time to spend for observing noble gas nucleation exceeds by far our simulation time. Thus
519 during the CO_2 degassing process, each noble gas atom behaves independently from each other and for

520 this reason they are used as independent tracers. We have checked this point by performing simulation
521 runs with a single noble gas atom and have found essentially the same results (except a poorer
522 statistics).

523 In order to follow the kinetics of bubble formation, we have evaluated as function of running time
524 the average elemental fraction (on an atomic basis), f_{CC} , of CO_2 molecules which are in the immediate
525 vicinity (first shell) of a carbon atom (this one belonging to a CO_2 molecule or to a CO_3^{2-} carbonate
526 ion, without distinction). The radius ($r_s=5A$) of the first shell around each carbon atom was chosen
527 empirically from an analysis of the atom-atom pair distribution functions, and we have checked that
528 the results are robust when changing its value on a limited range. During a decompression experiment
529 f_{CC} is expected to vary from a low or moderate value to a high value. Indeed, before decompression
530 each carbon atom of the CO_2 -saturated melt is surrounded primarily by the elements of the silicate,
531 whereas after the pressure drop a majority of CO_2 molecules are in the bubble.

532 To improve the statistics, our results were averaged over a series of 20 independent decompression
533 experiments (each one long of 5ns). For illustration, the time evolution of f_{CC} is shown in Fig.8 for a
534 100→10 kbar pressure drop. Before the pressure drop the value of f_{CC} in the CO_2 -saturated melt at
535 equilibrium is ~0.40 (a rather high value because the CO_2 content is ~29wt% at 100 kbar), and after
536 the pressure drop f_{CC} increases rapidly to reach a plateau value, ~0.76, after about 2,000 ps. This
537 evolution of f_{CC} is the signature of CO_2 bubble formation as shown by the correlated evolution of the
538 vesicularity of the simulated sample (see V^* in Fig.8). Indeed, when a bubble nucleates and grows,
539 the silicate atoms surrounding a carbon atom are progressively replaced by CO_2 molecules. Notice that
540 in a bulk CO_2 fluid f_{CC} is equal to one, but in our simulations the high surface/volume ratio of the
541 nanobubble modifies this value (hence $f_{CC}<1$). As a matter of fact, the CO_2 molecules in contact with
542 the melt at the surface of the bubble represent a significant proportion of the bubble forming molecules
543 (~40% for a bubble of 40A in diameter).

544 A quick glance at Fig.8 reveals that the time evolution of f_{CC} (and V^* as well) exhibits two different
545 regimes: a rapid evolution of great amplitude at short times ($0<t<100$ ps) followed by a slower

546 evolution of a much weaker amplitude at long times ($100 < t < 2,000$ ps). This time evolution is well
 547 described by the following bi-exponential function,

$$548 \quad f_{CC} = (f_{CC}^{min} - f_{CC}^{max})e^{-t/\tau_1} + f_{CC}^{inter}(e^{-t/\tau_2} - e^{-t/\tau_1}) + f_{CC}^{max} \quad (10)$$

549 where f_{CC}^{min} , f_{CC}^{inter} and f_{CC}^{max} are fitting parameters and τ_1 and τ_2 are time constants (the curve fitting
 550 shown in Fig.8 corresponds to the following parameters: $f_{CC}^{min} = 0.40$, $f_{CC}^{inter} = 0.04$, $f_{CC}^{max} = 0.76$,
 551 $\tau_1 = 60$ ps and $\tau_2 = 600$ ps). The two time constants give an estimate of the bubble growth rate at
 552 the nanometric scale. The time constant τ_1 , associated with the short time evolution, corresponds to
 553 the time spent for the formation of a critical nucleus, i.e. a cluster in which a central CO_2 molecule has
 554 essentially CO_2 molecules as first neighbors. On the other hand, the time constant τ_2 gives an estimate
 555 of bubble growth at long time. It expresses the coalescence time of critical nuclei and the expansion
 556 duration of bubble growth. Notice that the bubble ceases to grow after about 2,000 ps, when the melt
 557 super saturation in CO_2 molecules is exhausted, i.e. when the chemical equilibrium between the
 558 silicate melt and the CO_2 phase is achieved. Consequently the size of the bubble depends on the size of
 559 the simulated sample but the vesicularity does not.

560 Although our simulation gives information on bubble formation at the nanometric scale, for the sake
 561 of completeness it is useful to compare this microscopic description with a macroscopic point of view
 562 as given by classical nucleation theory. In this framework, for early-stage bubble growth when the
 563 surface/volume ratio is large, growth is limited by the viscosity of the melt (Prousevitch et al., 1993;
 564 Toramaru, 1995; Navon et al., 1998), and the bubble radius grows exponentially with time,

$$565 \quad R(t) \approx \exp\left[\frac{\Delta P}{4\eta} t\right] \quad (11)$$

566 where ΔP is the difference between the volatile pressure inside the bubble and the ambient pressure
 567 (equated to the pressure drop in a first approximation) and η the melt viscosity. In our simulation, the
 568 volume of an initial nucleus being proportional to the number of incoming CO_2 molecules, the latter

569 one grows approximately as $R^3(t)$. From the analogy between the microscopic definition expressed by
 570 Eq.(10) and the macroscopic relationship given by Eq.(11) one can deduce the following relation,

$$571 \quad \tau_1 \sim \frac{4\eta}{3\Delta P} \quad (12)$$

572 where τ_1 is the formation time of a critical nucleus. For the decompression experiment presented in
 573 Fig.8, the Eq.(12) leads to $\tau_1 = 6.7$ ps in using $\Delta P = 90$ kbar and $\eta = 0.045$ Pa.s for the viscosity of our
 574 CO_2 -bearing MORB melt evaluated at 1873K and 10 kbar (notice that the viscosity of our simulated
 575 melt is much lower than that of a real basaltic melt, by roughly a factor of ten at 1873 K, for a
 576 discussion see Bauchy et al. (2012), but this is immaterial in the present context). But this value of τ_1
 577 is about 9 times shorter than the result of the simulation ($\tau_1^{sim} = 60$ ps), a finding which implies that the
 578 simulation and the nucleation theory do not probe the same process or that the strict application of
 579 Eq.(11) is doubtful over a time scale of a few ps (for instance the relaxation time for the viscosity is
 580 much larger than a ps). Moreover the Eq.(11) is valid so long as a well formed interface between the
 581 CO_2 bubble and the silicate melt can be identified, and this is not yet the case when the system is made
 582 of scattered clusters. Nevertheless, for nucleation theory, the scale of the critical nucleus radius (given
 583 by $2\gamma/P$, where $\gamma \sim 0.36$ N/m is the surface tension for molten basalt as evaluated by Walker and
 584 Mullins, 1981), is about 3.8Å at $P=10$ kbar, a value which agrees well with the size of clusters
 585 observed in our simulation during the early stage of bubble formation. Moreover, the nucleation time
 586 τ_1 increases strongly when the volatile initial concentration becomes lower or when the pressure drop
 587 is decreased (e.g. τ_1 evolves from ~ 60 ps to ~ 230 ps when ΔP varies from 90 to 50 kbar). All these
 588 findings are in a qualitative agreement with classical nucleation theory (Proussevitch and Sahagian,
 589 1998) which predicts a slowing down of bubble growth at once with lower volatile oversaturation and
 590 with lower initial volatile concentration.

591 For noble gases we have proceeded similarly by defining the average fractions in CO_2
 592 molecules, f_{HeC} and f_{ArC} , within a sphere of radius 5Å centered on a *He* or an *Ar* atom. As illustrated
 593 in Fig.8, an important result is that the time evolutions of f_{HeC} and f_{ArC} are not only very similar to

594 each other but they are virtually identical to that of f_{CC} . More precisely they can be described by
 595 Eq.(10) with $\tau_1^{He} \approx \tau_1^{Ar} (\approx \tau_1^C) = 60 \text{ ps}$, $\tau_2^{He} \approx \tau_2^{Ar} (\approx \tau_2^C) = 600 \text{ ps}$, $f_{HeC}^{min} = 0.42$, $f_{HeC}^{inter} = 0.04$,
 596 $f_{HeC}^{max} = 0.78$, $f_{ArC}^{min} = 0.50$, $f_{ArC}^{inter} = 0.04$, and $f_{ArC}^{max} = 0.83$. Moreover, there is no time lag between
 597 the rises of f_{HeC} and f_{ArC} and that of f_{CC} , they are concomitant with each other. In other words, as
 598 soon as nucleation takes place, the *He* and *Ar* atoms located nearby a nucleation locus attach to it and
 599 become observers of its evolution. At the scale of our simulation (the simulation cell is a few nm long)
 600 the transfer of *He* and *Ar* atoms from the melt to a CO_2 bubble is achieved before the latter one is fully
 601 developed. There is no quantitative difference between *He* and *Ar* even if *He* atoms are more mobile
 602 than *Ar* atoms in the melt (at 1873K and 10 kbar their respective diffusion coefficients differ by
 603 roughly one order of magnitude: $D_{He} \sim 10^{-8} \text{ m}^2/\text{s}$ and $D_{Ar} \sim 1.5 \cdot 10^{-9} \text{ m}^2/\text{s}$ after our own evaluation). In
 604 fact the limiting step is the nucleation process itself and the noble gases present in the halo
 605 surrounding a nucleation locus stick to it and works one's way into it. A 3D visualization of the atomic
 606 trajectories into the simulation box is fully illustrative on this point (see Fig.7).

607 After the formation of the nanobubble is completed (equilibrium), it is observed along the
 608 simulation run that the rapid diffusion of a *He* atom into the CO_2 bubble leads from time to time to
 609 brief excursions of the noble gas atom into the bulk melt. This behavior is expected because the
 610 melt/ CO_2 partition coefficient of a *He* atom being equal to about 3% at 5 kbar (see Fig.3), in a highly
 611 vesiculated basaltic melt ($V^* \sim 0.3$ in the exemple of Fig.7) the noble gas will spent approximately
 612 $\sim 3\%$ of its time in the bulk melt and $\sim 97\%$ in the CO_2 bubble. For *Ar* atoms the partition coefficient is
 613 ten times smaller ($\sim 0.3\%$ at 5 kbar, see Fig.3) and indeed we observe very scarcely an excursion of an
 614 *Ar* atom out of the bubble. In summary, during a degassing episode the noble gas atoms present in the
 615 halo surrounding an incipient CO_2 bubble are transferred in the latter one at the same rate than the CO_2
 616 molecules themselves. So, when bubble growth is ended (or stopped) the concentration in noble gases
 617 becomes stationary and its value in the vesicles can be evaluated from Eq.(5) in introducing for V^* the
 618 current vesicularity.

619 Although our calculations were performed at the nanometric scale we believe that the conclusions
 620 which can be inferred are meaningful at the macroscopic scale. Thus, our results don't support the
 621 hypothesis that a kinetic fractionation between *He* and *Ar* is at the origin of the high *He/Ar* ratio
 622 observed in vesicles of some MORB samples (Aubaud et al., 2004). According to this hypothesis, the
 623 transfer of noble gases from the melt to the bubbles is considered as decoupled from the very process
 624 of bubble formation. When degassing is taking place, the *He* atoms diffusing faster than *Ar* atoms into
 625 the melt, the CO_2 bubbles (assumed to be depleted in noble gases) would be transiently enriched in *He*
 626 atoms with respect to *Ar* atoms, a disequilibrium leading to increase the *He/Ar* ratio in the vesicles.
 627 Furthermore, if the magma erupts before degassing is completed (due to a rapid ascent rate for
 628 instance) the high *He/Ar* ratio can be imprinted in the MORB glass (Paonita and Martelli, 2006). Our
 629 results show that the prerequisite of this scenario (the decoupling between bubble formation and noble
 630 gas transfer) is unrealistic. As a matter of fact, the noble gases are present from the formation of
 631 critical nuclei and consequently their abundances in the vesicles are controlled by the current
 632 vesicularity of the sample. For instance, a MORB melt CO_2 -saturated at 0.8 kbar and erupting at 3,000
 633 m.b.s.l. (i.e. $P_{erup} \sim 0.3$ kbar) will exhibit at equilibrium a vesicularity about 1% (see Fig.1). In this case
 634 the *He/Ar* ratio in the vesicles (see Fig.4) is equal to $\sim 0.4(C_0^{He}/C_0^{Ar})$ where C_0^{He} and C_0^{Ar} are the noble
 635 gas contents before vesiculation (notice that C_0^{He}/C_0^{Ar} may vary with the source region, see the
 636 discussion in section 3.2). But if during magma ascent, the CO_2 exsolution is delayed up to a super
 637 saturation ratio $\alpha=2.6$ is reached (for exemple), then the vesicularity at eruption is as low as $\sim 1.5 \cdot 10^{-4}$
 638 and the corresponding *He/Ar* ratio is equal to $\sim 0.1(C_0^{He}/C_0^{Ar})$. Thus, for a closed system degassing, the
 639 higher the CO_2 super saturation ratio the lower the *He/Ar* ratio in the vesicles at a given pressure
 640 (because *He* is more soluble than *Ar* in the silicate melt). Even if some *He* and *Ar* atoms of the melt
 641 are sufficiently distant from vesicles for migrating with delay in the latter ones, the incoming fluxes in
 642 noble gases are compensated by outgoing fluxes to fulfill equilibrium (Fick's law). In summary, an
 643 incomplete degassing lowers the vesicularity (with respect to a complete degassing) and diminishes
 644 the *He/Ar* ratio in the vesicles. So, to reconcile theory and observation (MORB samples exhibiting a
 645 low vesicularity and a strong CO_2 super saturation are generally displaying a high *He/Ar* ratio in the

646 vesicles) one must put forward other mechanisms capable of producing high C_0^{He}/C_0^{Ar} ratio in the melt
647 before the last vesiculation episode. We think that the sequential degassing mechanism with vesicle
648 loss, presented in section 3.2, can solve this outstanding question.

649 5. Conclusions

650 In this paper it has been shown that several aspects of MORB degassing can be described
651 realistically by atomistic simulations. The main results of this study are the following.

652 1- In using a force field developed by Guillot and Sator (2011) to model by MD simulation the
653 incorporation of CO_2 into silicate melts, the vesicularity of a MORB melt has been evaluated as
654 function of initial CO_2 contents and pressure at eruption. An excellent agreement is obtained between
655 calculated values and vesicularity data of MORB samples collected at mid-ocean ridges. This
656 comparison also indicates that most of MORB samples have experienced a last vesiculation episode at
657 shallow depth ($d < 15$ km) in the oceanic mantle. In contrast, a few highly vesicular samples (e.g.
658 *popping rocks*) could be issued from deep-seated CO_2 -rich magmas. A possible origin of the latter
659 ones are CO_2 -rich silica-undersaturated melts (e.g. carbonatite-like) in transit through the oceanic
660 mantle which, in assimilating the silicate matrix, could drive the melt to a basaltic composition. If their
661 CO_2 content is sufficiently high, the MORB melt may exsolve a great amount of CO_2 leading in
662 special cases to a submarine explosive volcanism. For instance, according to our results, the
663 vesicularity of a MORB composition with 9.5 wt% CO_2 reaches the fragmentation threshold
664 ($V^* \sim 0.75$) at a water depth of 4,000 m whereas a MORB melt with 4.6 wt% CO_2 will experience an
665 explosive fragmentation in erupting at 1,500 m.b.s.l. In short, the possibility that CO_2 -rich magmas
666 may drive explosive volcanism at some mid-ocean ridges has been underestimated up to now.

667 2- The evaluation of the pressure dependence of the noble gas partition coefficients between a MORB
668 melt and a supercritical CO_2 phase shows that noble gas transfer from the silicate melt to the CO_2
669 phase is hindered at high pressure by the density of the fluid. Thus, the partition coefficients of He and
670 Ar increase by a factor of about 4~5 between 0 and 50 kbar. So MORB degassing at great depth would

671 be less efficient than expected to deplete the upper mantle in noble gases. Furthermore it is shown that
672 the large distribution in Ar contents and of the He/Ar ratio measured in MORB samples can be
673 explained if the ascending magma experiences a series of vesiculation at depth followed by vesicle
674 loss.

675 3- By performing a decompression numerical experiment where a pressure drop is applied to a volatile
676 (CO_2 +noble gas) bearing MORB melt, it is possible to investigate (and to visualize) the formation of
677 critical nuclei leading to CO_2 bubble formation. Interestingly, noble gases present in the neighborhood
678 of nucleation loci exhibit a great affinity for CO_2 clusters. In fact, the transfer of noble gases from the
679 melt to these embryos is so effective that the transfer rate in a growing CO_2 bubble is identical to that
680 of the CO_2 molecules themselves. Thus, when bubble growth is stopping the concentration of vesicles
681 in noble gases becomes stationary and is a function of the current vesicularity (see Eq.(4)). This
682 finding doesn't support the hypothesis that a kinetic fractionation between *He* and *Ar* (induced by their
683 diffusivity difference in the melt) is at the origin of the high *He/Ar* ratio observed in vesicles of some
684 MORB samples.

685

686 **Acknowledgements**

687 Bertrand Guillot and Nicolas Sator acknowledge the Agence Nationale pour la Recherche (under
688 Grant agreement ANR-2010-BLAN-621-03) and the European Research Council (under Grant
689 agreement N°279790).

690

691

692

693

694

695

696

697

698

699

Table 1

700 Simulation conditions. All simulations were performed at 1873K. In the table below, the simulated
 701 MORB melt is composed of 5,000 ions plus the number of CO_2 molecules, $(N_{CO_2})_{melt}$, necessary to
 702 reach CO_2 -saturation (indicated by W) at the investigated pressure. The density of the CO_2 -saturated
 703 MORB is given by n_{melt} and that of the coexisting supercritical CO_2 phase by n_{CO_2} . To evaluate the
 704 system size dependence, the calculations were also performed with a smaller system where the MORB
 705 was composed of only 1,000 ions plus the corresponding number of CO_2 molecules (in that case
 706 $(N_{CO_2})_{melt}$ reported below has to be divided by 5). As for the pure CO_2 phase, it was also simulated
 707 with two system sizes, a large system with 2,500 CO_2 molecules and a smaller one with 500
 708 molecules.

709	P(kbar)	$W(g_{CO_2}/g_{melt})$	$(N_{CO_2})_{melt}$	$n_{melt}(g/cm^3)$	$n_{CO_2}(g/cm^3)$
710	0.001	$5 \cdot 10^{-7}$	0	2.63	$3 \cdot 10^{-4}$
711	10	0.006	15	2.74	0.94
712	20	0.016	40	2.83	1.21
713	30	0.046	120	2.88	1.38
714	50	0.095	275	2.99	1.60
715	80	0.21	660	3.07	1.81
716	100	0.29	1065	3.09	1.91

717

718

719

720

721

722

Table 2

723 Pressure dependence of noble gas solubility parameters in the CO_2 -saturated MORB melt (γ_m^i) and in
 724 the coexisting supercritical CO_2 phase ($\gamma_{CO_2}^i$) at 1873K. Values calculated with the two system sizes
 725 are indicated: S is for small system sizes and L is for large system sizes (see Table 1 for the number of
 726 atoms in each system). For each investigated pressure, the reference value of the solubility parameter
 727 (noted *mean*) is given by the arithmetic mean of the S and L values. Notice that the evaluation of γ_m^{Xe}
 728 becomes inaccurate from 30 kbar whereas that of $\gamma_{CO_2}^{Xe}$ is accurate up to 80 kbar.

729	P(kbar)		γ_m^{He}	$\gamma_{CO_2}^{He}$	γ_m^{Ne}	$\gamma_{CO_2}^{Ne}$	γ_m^{Ar}	$\gamma_{CO_2}^{Ar}$	γ_m^{Xe}	$\gamma_{CO_2}^{Xe}$
730	-----									
731										
732	0.001	S	1.83(-2)	1.0	9.81(-3)	1.0	1.47(-3)	1.0	2.88(-4)	1.0
733		L	1.83(-2)	1.0	9.81(-3)	1.0	1.47(-3)	1.0	2.88(-4)	1.0
734		<i>mean</i>	<i>1.83(-2)</i>	<i>1.0</i>	<i>9.81(-3)</i>	<i>1.0</i>	<i>1.47(-3)</i>	<i>1.0</i>	<i>2.88(-4)</i>	<i>1.0</i>
735										
736	10	S	5.49(-3)	1.71(-1)	2.87(-3)	1.39(-1)	1.96(-4)	6.60(-2)	1.39(-5)	3.21(-2)
737		L	5.56(-3)	1.72(-1)	2.97(-3)	1.39(-1)	2.18(-4)	6.67(-2)	1.40(-5)	3.26(-2)
738		<i>mean</i>	<i>5.53(-3)</i>	<i>1.72(-1)</i>	<i>2.92(-3)</i>	<i>1.39(-1)</i>	<i>2.07(-4)</i>	<i>6.64(-2)</i>	<i>1.40(-5)</i>	<i>3.24(-2)</i>
739										
740	20	S	2.81(-3)	6.17(-2)	1.25(-3)	4.23(-2)	4.50(-5)	1.03(-2)	1.20(-6)	2.59(-3)
741		L	2.87(-3)	6.18(-2)	1.28(-3)	4.24(-2)	4.92(-5)	1.04(-2)	1.26(-6)	2.62(-3)
742		<i>mean</i>	<i>2.84(-3)</i>	<i>6.18(-2)</i>	<i>1.27(-3)</i>	<i>4.24(-2)</i>	<i>4.71(-5)</i>	<i>1.04(-2)</i>	<i>1.23(-6)</i>	<i>2.61(-3)</i>
743										
744	30	S	1.54(-3)	2.72(-2)	5.91(-4)	1.60(-2)	1.14(-5)	2.11(-3)	9.31(-8)	2.91(-4)
745		L	1.59(-3)	2.70(-2)	6.12(-4)	1.59(-2)	1.35(-5)	2.11(-3)	3.24(-7)	2.92(-4)
746		<i>mean</i>	<i>1.57(-3)</i>	<i>2.71(-2)</i>	<i>6.02(-4)</i>	<i>1.60(-2)</i>	<i>1.25(-5)</i>	<i>2.11(-3)</i>	<i>2.09(-7)</i>	<i>2.92(-4)</i>
747										
748	50	S	5.21(-4)	6.66(-3)	1.49(-4)	2.97(-3)	9.94(-7)	1.27(-4)	1.05(-8)	5.92(-6)
749		L	5.31(-4)	6.78(-3)	1.54(-4)	3.04(-3)	1.18(-6)	1.33(-4)	6.26(-8)	6.13(-6)
750		<i>mean</i>	<i>5.26(-4)</i>	<i>6.72(-3)</i>	<i>1.52(-4)</i>	<i>3.01(-3)</i>	<i>1.09(-6)</i>	<i>1.30(-4)</i>	<i>3.66(-8)</i>	<i>6.03(-6)</i>
751										
752	80	S	1.19(-4)	1.18(-3)	2.33(-5)	3.65(-4)	2.84(-8)	3.59(-6)	n.e.	4.08(-8)
753		L	1.19(-4)	1.19(-3)	2.34(-5)	3.67(-4)	4.61(-8)	3.67(-6)	n.e.	3.43(-8)
754		<i>mean</i>	<i>1.19(-4)</i>	<i>1.19(-3)</i>	<i>2.34(-5)</i>	<i>3.66(-4)</i>	<i>3.73(-8)</i>	<i>3.63(-6)</i>	<i>n.e.</i>	<i>3.76(-8)</i>
755										
756	100	S	4.63(-5)	4.19(-4)	7.70(-6)	1.03(-4)	3.94(-9)	3.50(-7)	n.e.	1.73(-9)
757		L	4.78(-5)	4.19(-4)	7.89(-6)	1.02(-4)	6.00(-9)	3.02(-7)	n.e.	4.37(-10)
758		<i>mean</i>	<i>4.71(-5)</i>	<i>4.19(-4)</i>	<i>7.80(-6)</i>	<i>1.03(-4)</i>	<i>4.97(-9)</i>	<i>3.26(-7)</i>	<i>n.e.</i>	<i>1.08(-9)</i>

759 n.e. not evaluated

761

762

Figure captions

763

764 **Fig.1** Pressure dependence of the vesicularity of an ascending magma as described by our simulated
 765 MORB melt at 1873K and for different initial CO_2 contents at depth (namely 0.06, 0.3, 0.6, 1.6, 4.6,
 766 9.5, 21 and 29 wt% corresponding to $P_{CO_2}^{sat} = 1, 5, 10, 20, 30, 50, 80$ and 100 kbar). The full curves
 767 correspond to a super saturation ratio $\alpha=1$, and the dotted curves to $\alpha=2$ (see text). Symbols represent
 768 the vesicularity of MORB samples collected on the Atlantic (squares), Indian (triangles) and Pacific
 769 (crosses) ridges (data are from Chavrit (2010), Hekinian et al. (2000) and Pineau et al. (2004)). Values
 770 of the initial CO_2 contents (in wt% CO_2) are indicated along the curves.

771 **Fig.2** Vesicularity of our simulated MORB evaluated at 1,000 m.b.s.l. (upper set of red dots, color
 772 online) and at 5,000 m.b.s.l. (lower set of red dots, color online) as function of the initial CO_2 content
 773 before degassing (the corresponding CO_2 -saturation pressure is indicated on the upper axis). Data for
 774 MORB samples dredged between $\sim 1,000$ m.b.s.l. and 5,400 m.b.s.l. on the Atlantic (squares), Indian
 775 (triangles), and Pacific (crosses) ridges are shown for comparison (data source: Chavrit (2010) and
 776 Pineau et al. (2004)). Notice that the CO_2 content in the (bulk) saturated melt at 1,000 m.b.s.l. is about
 777 50 ppmw, and is about 250 ppmw at 5,000 m.b.s.l., values which become non negligible with respect
 778 to the CO_2 content in vesicles only when the vesicularity is very low ($V^* \leq 10^{-3}$).

779 **Fig.3** MORB- CO_2 noble gas partition coefficients as function of pressure. The dotted curves represent
 780 the raw results obtained with small system sizes (lower curve) and with large system sizes (upper
 781 curve), respectively, whereas the full curves are obtained from their arithmetic mean. The separation
 782 between the two dotted curves gives an estimation of the error bar (see text and Table 2). Notice that
 783 the distinction between dotted curves and full curves is barely visible for He and Ne over the entire
 784 pressure range. For Xe the results become unreliable above 30 kbar and are not shown (see Table 2).

785 **Fig.4** 4He and ^{40}Ar contents in melt (m) and in vesicles (v) as function of the vesicularity evaluated at
 786 an hydrostatic pressure equivalent to 3,000 m.b.s.l.. The abundances in noble gases are normalized

787 with their initial values in the undegassed sample. The total CO_2 content of the MORB melt is
 788 indicated by a number which corresponds to the CO_2 -saturation pressure, $P_{CO_2}^{sat}$, given in kbar.

789 **Fig.5** Ar content in vesicles (in $10^{-6} \text{ g}_{Ar}/\text{g}_{melt}$ or ppmw) as function of the vesicularity evaluated at
 790 3,000 m.b.s.l.. The initial abundance in ^{40}Ar of the source region is assumed to be equal to that
 791 measured in the $2\pi D43$ *popping rock* (~ 0.1 ppmw, Moreira et al. (1998)) whereas different initial
 792 conditions of CO_2 -saturation are investigated (namely $P_{CO_2}^{sat} = 0.4, 0.5, 0.6, 0.7, 0.8, 0.9, 1, 2, 3, 4, 5, 10,$
 793 $20, 30, 40$ and 50 kbar). The numbers associated with arrows indicate the value of $P_{CO_2}^{sat}$. The curve
 794 labeled V^1 , and corresponding to the red dots (color on line), describes a closed system degassing
 795 without vesicle loss. The curves labeled V^2 (blue dots) describe a 2-stage vesiculation process with
 796 vesicle loss. For illustration, three degassing paths are shown: ($P_1=20; P_2=19, 18, \dots, 0.4$ kbar), ($P_1=5;$
 797 $P_2=4, 3, \dots, 0.4$ kbar) and ($P_1=1; P_2= 0.9, 0.8, \dots, 0.4$ bar) where P_1 is the pressure at which the first
 798 vesiculation stage occurs and P_2 the pressure of the second vesiculation stage, knowing that in
 799 between the ascending magma has experienced a total loss of vesicles. For 3-stage vesiculation
 800 (labeled V^3 and green dots), and 4-stage vesiculation (labeled V^4 and cyan dots), for the sake of clarity
 801 only one degassing path is shown: ($P_1=20; P_2=3; P_3=2, 1, \dots, 0.4$ kbar) and ($P_1=20; P_2=3; P_3= 1; P_4=0.9,$
 802 $0.8, \dots, 0.4$ kbar). Notice that most of the experimental data (black squares, data taken from Chavrit
 803 (2010)) can be explained by a 2-, 3- or 4- stage vesiculation process, whereas the $2\pi D43$ *popping rock*
 804 is well described by a closed system degassing starting at 10 kbar (i.e. ~ 30 km in the oceanic mantle).

805 **Fig.6** As in Fig.5 but for the $^4He/^{40}Ar$ ratio. The $^4He/^{40}Ar$ ratio of the source region is assumed to be
 806 identical to that of the $2\pi D43$ *popping rock* (~ 1.5 , see Moreira et al. (1998)).

807 **Fig.7** Snapshots of the simulation cell during a decompression experiment. Picture (a) shows a
 808 snapshot of the simulation cell containing a MORB melt CO_2 -saturated at 1873K and 50 kbar. The
 809 system is composed of 5,000 silicate atoms, 275 CO_2 molecules (in fact ~ 99 CO_2 molecules and ~ 176
 810 carbonate ions, CO_3^{2-} , on average) and one He atom. For clarity, the size of the silicate atoms are
 811 arbitrarily reduced with respect to that of the CO_2 molecules (carbon atoms are in blue, oxygen atoms

812 are in red and carbonate ions appear as bent CO_2 molecules) whereas the size of the He atom (in
 813 yellow) is magnified. Notice that the distribution of CO_2 molecules within the melt is homogeneous
 814 and that the He atom is not preferentially solvated by CO_2 molecules. The system is suddenly
 815 decompressed from 50 to 5 kbar and it is observed, in picture (b), at a time $t=250$ ps after the pressure
 816 drop. On this snapshot most of the CO_2 molecules are forming clusters: one is visible near the center
 817 of the box and another one, solvating the He atom, is located on the right side of the box. After 5,450
 818 ps (picture (c)) all the nuclei have clustered together in a unique bubble in which the He atom is
 819 enclosed. The final vesicularity of the system is about $\sim 30\%$ as expected from thermodynamics (see
 820 Fig.1 for a 50 \rightarrow 5 kbar decompression path).

821 **Fig.8** Kinetics of bubble formation and noble gas transfer during a decompression experiment. The
 822 initial state is a well equilibrated MORB melt CO_2 -saturated at 100 kbar and 1873K, and the final state
 823 is a vesiculated melt at 10 kbar and 1873K. The decompression step (100 \rightarrow 10 kbar) takes place at $t=0$
 824 and is quasi instantaneous (the pressure drop is applied over one MD step, i.e. 0.001 ps). The figure
 825 shows as function of running time the evolution of the atomic fraction in CO_2 molecules which are in
 826 the immediate neighborhood of a CO_2 molecule, f_{CC} , of a He atom, f_{HeC} , and of an Ar atom, f_{ArC} . The
 827 raw data are the wiggling curves (blue for CO_2 , red for He and green for Ar , color online) whereas the
 828 black dotted curves are least squared fits based upon a bi-exponential function (see text and Eq.(10)).
 829 The statistical noise of the raw data is much larger with He and Ar than with CO_2 because the number
 830 of CO_2 molecules in the simulated sample is much larger than that of the noble gases (213 instead of
 831 10). Notice that for $t>0$ the three functions f_{CC} , f_{HeC} , and f_{ArC} exhibit a quasi identical steep rise at short
 832 times without time lag, suggesting that bubble formation and noble gas catchment are simultaneous.
 833 The time evolution of the vesicularity V^* is also shown for comparison (thick black curve). Notice
 834 that the vesicularity of the sample reaches a plateau value equal to 0.534 which is precisely the value
 835 expected from thermodynamics at equilibrium (Eq.(7)). For a rapid check, read in Fig.1 the value of
 836 the vesicularity at 10 kbar for an ascending melt saturated at 100 kbar (the curve marked 29 wt% in
 837 Fig.1).

838

Appendix

839 To describe the noble gas- CO_2 interactions, we have used the molecular models for binary mixtures
 840 developed by Vrabec et al. (2001, 2009) where the pair potential between a noble gas atom X and a
 841 CO_2 molecule is given by a sum of two Lennard-Jones (L-J) potentials,

$$842 \quad u_{X,CO_2} = \sum_{n=1,2} 4\varepsilon_{XO} \left[\left(\frac{\sigma_{XO}}{r_{XO_n}} \right)^{12} - \left(\frac{\sigma_{XO}}{r_{XO_n}} \right)^6 \right] \quad (A1)$$

843 where ε_{XO} and σ_{XO} are L-J parameters and r_{XO_n} is the distance between the noble gas atom X and one
 844 of the two oxygen atoms ($n=1,2$) belonging to the CO_2 molecule. The interaction between the noble
 845 gas and the carbon atom is not considered because the latter one is deeply embedded into the
 846 electronic clouds of the oxygen atoms. Trial values for ε_{XO} and σ_{XO} are deduced from the Lorentz-
 847 Berthelot combining rules,

$$848 \quad \sigma_{XO} = \frac{\sigma_X + \sigma_O}{2} \quad (A2)$$

$$849 \quad \varepsilon_{XO} = \sqrt{\varepsilon_X \varepsilon_O} \quad (A3)$$

850 where σ_X , σ_O , ε_X and ε_O are L-J parameters describing the pure fluids (for He , see Dykstra (1989), and
 851 for Ne , Ar and Xe , see Vrabec et al. (2001). Although the Lorentz-Berthelot combining rules are
 852 widely used to model binary mixtures, there is room for improvement. So, we have followed the
 853 procedure of Huang et al. (2009) which consists in introducing an adjustable parameter, ξ_X , in the
 854 Lorentz-Berthelot rule for the pair energy parameter,

$$855 \quad \varepsilon_{XO} = \xi_X \sqrt{\varepsilon_X \varepsilon_O}, \quad (A4)$$

856 to reproduce at best Henry's constant of noble gases in liquid CO_2 .

857 From a computational standpoint, Henry's constant, H_X , of a noble gas X in a liquid solvent S writes
 858 (Shing et al., 1988)

$$859 \quad H_X = \rho k_B T / \gamma_S^X = \rho k_B T \times e^{\frac{\mu_S^{X,ex}}{k_B T}} \quad (A5)$$

860 where ρ is the numerical density of the solvent (e.g. CO_2), T the temperature, k_B the Boltzmann
 861 constant, and γ_S^X the solubility parameter of the noble gas X in the solvent. We have evaluated the
 862 Henry constant of He, Ne, Ar and Xe in liquid CO_2 at 273K by implementing the TPM (see Eq.(8)).
 863 Computational details are the same as those given in section 2.3. Thus, the simulated liquid sample is
 864 composed of 500 CO_2 molecules interacting through the Zhang and Duan potential (2005) modified by
 865 Guillot and Sator (2011) for bending, and the insertion energy of the noble gas atom in liquid CO_2 is
 866 calculated with the pair potential described above. For each noble gas, the Henry constant is evaluated
 867 via Eq.(A5) in adjusting by trial and error the parameter, ξ_X , to reproduce at best the noble gas
 868 solubility data of the literature. Final values of the L-J potential parameters for noble gas- CO_2
 869 interactions are given in Table A1 as also as the comparison between calculated and measured Henry's
 870 constants.

871 **Table A1**

872 L-J potential parameters for noble gas- CO_2 interactions and comparison between calculated and
 873 experimental values for the Henry constant at 273K.

874	X	σ_{XO} (Å)	ε_{XO} (kJ/mol)	H_X^{calc} (bar)	H_X^{exp} (bar)
875	<i>He</i>	2.81	0.525	$2.0 \pm 0.2 \cdot 10^3$	^a $2.05 \pm 0.35 \cdot 10^3$
876	<i>Ne</i>	2.89	0.671	$1.5 \pm 0.2 \cdot 10^3$	^b $1.2 \pm 0.2 \cdot 10^3$
877	<i>Ar</i>	3.19	1.131	$3.0 \pm 0.3 \cdot 10^2$	^c $3.4 \pm 0.6 \cdot 10^2$
878	<i>Xe</i>	3.44	1.317	90 ± 10	^d 87

879 a Mackendrick et al., 1968

880 b Sasinovskii, 1979

881 c Kaminishi et al., 1968

882 d Ackley and Notz, 1976

883

884

885

BIBLIOGRAPHY

886 Ackley R.D. and Notz K.J. (1976) Distribution of xenon between gaseous and liquid CO₂. Technical
887 Report ORNL-5122, Oak Ridge National Lab. TN (USA), 1-35.

888 Albarède F. (2008) Rogue mantle helium and neon. *Science* **319**, 943-945.

889 Allègre C.J., Staudacher T., Sarda P. and Kurz M. (1983) Constraints on evolution of Earth's mantle
890 from rare gas systematics. *Nature* **303**, 762-766.

891 Allègre C.J., Staudacher T. and Sarda P. (1986/87) Rare gas systematics, formation of the atmosphere,
892 evolution and structure of the Earth's mantle. *Earth Planet. Sci. Lett.* **81**, 127-150.

893 Anderson D.L. (1998) The helium paradoxes. *Proc. Natl. Acad. Sci. USA* **95**, 4822-4827.

894 Aubaud C., Pineau F., Jambon A. and Javoy M. (2004) Kinetic disequilibrium of C, He, Ar and carbon
895 isotopes during degassing of mid-ocean ridge basalts. *Earth and Planet. Sci. Lett.* **222**, 391-406.

896 Bauchy M., Guillot B., Micoulaut M. and Sator N. (2012) Viscosity and viscosity anomalies of model
897 silicates and magmas: a numerical investigation. *Chem. Geol.*,
898 <http://dx.doi.org/10.1016/J.chemgeo.2012.08.035>.

899 Bologna M.S., Padilha A.L., Vitorello I. and Pádua M.B. (2011) Signatures of continental collisions
900 and magmatic activity in central Brazil as indicated by a magnetotelluric profile across distinct
901 tectonic provinces. *Precambrian Res.* **185**, 55-64.

902 Botcharnikov R., Freise M., Holtz F. and Behrens H. (2005) Solubility of C-O-H mixtures in natural
903 melts: new experimental data and application range of recent models. *Annals of Geophys.* **48**, 633-
904 646.

905 Bottinga Y. and Javoy M. (1990) MORB degassing: Bubble growth and ascent. *Chem. Geol.* **81**, 255-
906 270.

907 Brooker R.A., Wartho J.-A., Carroll M.R., Kelley S.P. and Draper D.S. (1998) Preliminary UVLAMP
908 determinations of argon partition coefficients for olivine and clinopyroxene grown from silicate melts.
909 *Chem. Geol.* **147**, 185-200.

910 Brooker R.A., Kohn S.C., Holloway, J.R. and McMillan P.F. (2001) Structural controls on the
911 solubility of CO₂ in silicate melts Part I: bulk solubility data. *Chem. Geol.* **174**, 225-239.

- 912 Brooker R.A., Du Z., Blundy J.D., Kelley S.P., Allan N.L., Wood B.J., Chamorro E.M., Wartho J.-A.
913 and Purton J.A. (2003) The "zero charge" partitioning behaviour of noble gases during mantle melting.
914 Nature **423**, 738-741.
- 915 Burnard P. (1999) The bubble-by-bubble volatile evolution of two mid-ocean ridge basalts. Earth and
916 Planet. Sci. Lett. **174**, 199-211.
- 917 Burnard P. (2001) Correction for volatile fractionation in ascending magmas; noble gas abundances in
918 primary mantle melts, Geochim. Cosmochim. Acta **65**, 2605-2614.
- 919 Burnard P. (2004) Diffusive fractionation of noble gases and helium isotopes during mantle melting.
920 Earth Planet. Sci. Lett. **220**, 287-295.
- 921 Burnard P., Graham D. and Farley K. (2004) Fractionation of noble gases (He, Ar) during MORB
922 mantle melting: a case study on the Southeast Indian Ridge. Earth Planet. Sci. Lett. **227**, 457-472.
- 923 Cartigny P., Pineau F., Aubaud C. and Javoy M. (2008) Towards a consistent mantle carbon flux
924 estimate: Insights from volatile systematics (H_2O/Ce , δD , CO_2/Nb) in the North Atlantic mantle ($14^\circ N$
925 and $34^\circ N$). Earth Planet. Sci. Lett. **265**, 672-685.
- 926 Chamorro E.M., Wartho J.-A., Brooker R.A., Wood B.J., Kelley S.P. and Blundy J.D. (2002) Ar and
927 K partitioning between clinopyroxene and silicate melt to 8 GPa. Geochim. Cosmochim. Acta **66**, 507-
928 519.
- 929 Chavrit D. (2010) Global mapping of CO_2 fluxes along the Mid-Ocean Ridge system: a petrological
930 approach. PhD thesis, Université de Nantes (France).
- 931 Clague D.A., Paduan J.B. and Davis A.S. (2009) Widespread strombolian eruptions of mid-ocean
932 ridge basalt. J. Volcanol. Geotherm. Res. **180**, 171-188.
- 933 Colin A., Burnard P.G., Graham D.W. and Marrocchi Y. (2011) Plume-ridge interaction along the
934 Galapagos Spreading center: discerning between gas loss and source effects using neon isotopic
935 compositions and 4He - $^{40}Ar^*$ - CO_2 relative abundances. Geochim. Cosmochim. Acta **75**, 1145-1160.
- 936 Dalton J.A. and Presnall D.C. (1998) The continuum of primary carbonatitic-kimberlitic melt
937 compositions in equilibrium with lherzolite: Data from the system CaO - MgO - Al_2O_3 - SiO_2 - CO_2 at 6
938 GPa. J. Petrol. **39**, 1953-1964.
- 939 Dasgupta R. and Hirschmann M.M. (2006) Melting in the Earth's deep upper mantle caused by carbon
940 dioxide. Nature **440**, 659-662.

- 941 Deitrick G.L., Scriven L.E. and Davis H.T. (1989) Efficient molecular simulation of chemical-
942 potentials. *J. Chem. Phys.* **90**, 2370-2385.
- 943 Dixon J.E., Stolper E. and Delaney J.R. (1988) Infrared spectroscopic measurements of CO₂ and H₂O
944 in Juan de Fuca Ridge basaltic glasses. *Earth Planet. Sci. Lett.* **90**, 87-104.
- 945 Dixon J.E., Stolper E.M. and Holloway J.R. (1995) An experimental study of water and carbon
946 dioxide solubilities in mid-ocean ridge basaltic liquids Part I: Calibration and solubility models. *J.*
947 *Petrol.* **36**, 1607-1631.
- 948 Dixon J.E. (1997) Degassing of alkalic basalts. *Am. Mineral.* **82**, 368-378.
- 949 Dixon J., Clague D.A., Cousens B., Monsalve M.L. and Uhl J. (2008) Carbonatite and silicate melt
950 metasomatism of the mantle surrounding the Hawaiian plume: Evidence from volatiles, trace
951 elements, and radiogenic isotopes in rejuvenated-stage lavas from Niihau, Hawaii. *Geochem.*
952 *Geophys. Geosyst.* **9**, Q09005-1-34
- 953 Dykstra C.E. (1989) Molecular mechanics for weakly interacting assemblies of rare gas atoms and
954 small molecules. *J. Am. Chem. Soc.* **111**, 6168-6174.
- 955 Eggler D.H. (1976) Does CO₂ cause partial melting in the low-velocity layer of the mantle ?
956 *Geology* **4**, 69-72.
- 957 Eissen J.-Ph, Fouquet Y., Hardy D. and Ondréas H. (2003) Recent MORB volcanoclastic explosive
958 deposits formed between 500 and 1750 m.b.s.l. on the axis of the mid-atlantic ridge, south of the
959 Azores. In *Explosive Subaqueous Volcanism*, *Geophys. Monograph* **140**, 143-166.
- 960 Evans R.L., Hirth G., Baba K., Forsyth D., Chave A. and Mackie R. (2005) Geophysical evidence
961 from the MELT area for compositional controls on oceanic plates. *Nature* **437**, 249-252.
- 962 Gaillard F., Malki M., Iacono-Marziano G., Pichavant M. and Scaillet B. (2008) Carbonatite melts and
963 electrical conductivity in the asthenosphere. *Science* **322**, 1363-1365.
- 964 Gardner J.E., Hilton M. and M.R. Carroll (2000) Bubble growth in highly viscous silicate melts during
965 continuous decompression from high pressure. *Geochim. Cosmochim. Acta* **64**, 1473-1483.
- 966 Gonnermann H.M. and Mukhopadhyay S. (2009) Preserving noble gases in a convecting mantle.
967 *Nature* **459**, 560-564.
- 968 Graham D. and Sarda P. (1991) Mid-ocean ridge popping rocks: implications for degassing at ridge
969 crests - Comment. *Earth Planet. Sci. Lett.* **105**, 568-573.

- 970 Graham D.W. (2002) Noble gas isotope geochemistry of mid-ocean ridge and ocean island basalts:
971 Characterization of mantle source reservoirs. In *Noble Gases in Geochemistry and Cosmochemistry*
972 (eds. D. Porcelli, C.J. Ballentine and R. Wieler), *Reviews in Mineralogy and Geochemistry* **47**, 247-
973 319.
- 974 Guillot B. and Sarda P. (2006) The effect of compression on noble gas solubility in silicate melts and
975 consequences for degassing at mid-ocean ridges. *Geochim. Cosmochim. Acta* **70**, 1215-1230.
- 976 Guillot B. and Sator N. (2007a) A computer simulation study of natural silicate melts. Part I: Low
977 pressure properties. *Geochim. Cosmochim. Acta* **71**, 1249-1265.
- 978 Guillot B. and Sator N. (2007b) A computer simulation study of natural silicate melts. Part II: High
979 pressure properties. *Geochim. Cosmochim. Acta* **71**, 4538-4556.
- 980 Guillot B. and Sator N. (2011) Carbon dioxide in silicate melts: A molecular dynamics simulation
981 study. *Geochim. Cosmochim. Acta* **75**, 1829-1857.
- 982 Guillot B. and Sator N. (2012) Noble gases in high-pressure silicate liquids: A computer simulation
983 study. *Geochim. Cosmochim. Acta* **80**, 51-69.
- 984 Hammouda T. (2003) High-pressure melting of carbonated eclogite and experimental constraints on
985 carbon recycling and storage in the mantle. *Earth Planet. Sci. Lett.* **214**, 357-368.
- 986 Harper C.L. Jr. and Jacobsen S.B. (1996) Noble gases and Earth's accretion. *Science* **273**, 1814-1818.
- 987 Heber V.S., Brooker R.A., Kelley S.P. and Wood B. (2007) Crystal-melt partitioning of noble gases
988 (helium, neon, argon, krypton, and xenon) for olivine and clinopyroxene. *Geochim. Cosmochim. Acta*
989 **71**, 1041-1061.
- 990 Hékinian R., Chaigneau M. and Cheminée J.-L. (1973) Popping rocks and lava tubes from the Mid-
991 Atlantic rift valley at 36°N. *Nature* **245**, 371-373.
- 992 Hékinian R., Pineau F., Shilobreeva S., Bideau D., Garcia E. and Javoy M (2000) Deep sea activity on
993 the Mid-Atlantic Ridge near 34°50'N: Magma composition, vesicularity and volatile content. *J.*
994 *Volcanol. Geotherm. Res.* **98**, 49-77.
- 995 Helo C., Longpré M.-A., Shimizu N., Clague D.A. and Stix J. (2011) Explosive eruptions at mid-
996 ocean ridges driven by CO₂-rich magmas. *Nature Geoscience* **4**, 260-263.
- 997 Huang Y.-L., Miroshnichenko S., Hasse H. and Vrabec J. (2009) Henry's law constant from molecular
998 simulation: A systematic study of 95 systems. *Int. J. Thermophys.* **30**, 1791-1810.

- 999 Jambon A., Weber H. and Braun O. (1986) Solubility of He, Ne, Ar, Kr and Xe in a basalt melt in the
1000 range 1250-1600°C. *Geochemical implications. Geochim. Cosmochim. Acta* **50**, 401-408.
- 1001 Javoy M. and Pineau F. (1991) The volatiles record of a "popping" rock from the Mid-Atlantic Ridge
1002 at 14°N: chemical and isotopic composition of gas trapped in the vesicles. *Earth Planet Sci. Lett.* **107**,
1003 598-611.
- 1004 Jendrzejewski N., Trull T.W., Pineau F. and Javoy M. (1997) Carbon solubility in mid-ocean ridge
1005 basaltic melt at low pressures (250-1950 bar). *Chem. Geol.* **138**, 81-92.
- 1006 Kaminishi G.I., Arai Y., Saito S. and Maeda S. (1968) Vapor-liquid equilibria for binary and ternary
1007 mixtures containing carbon dioxide. *J. Chem. Eng. Jpn* **1**, 109-116.
- 1008 Mackendrick R.F., Heck C.K. and Barrick P.L. (1968) Liquid-vapor equilibria of the helium-carbon
1009 dioxide system. *J. Chem. Eng. Data.* **13**, 352-353.
- 1010 Marty B. and Tolstikhin I.N. (1998) CO₂ fluxes from mid-ocean ridges, arcs and plumes. *Chem. Geol.*
1011 **145**, 233-248.
- 1012 Marty B. and Zimmermann L. (1999) Volatiles (He, C, N, Ar) in mid-ocean ridge basalts: Assessment
1013 of shallow-level fractionation and characterization of source composition. *Geochim. Cosmochim. Acta*
1014 **63**, 3619-3633.
- 1015 Meibom A., Anderson D.L., Sleep N.H., Frei R., Chamberlain C.P., Hren M.T. and Wooden J.L.
1016 (2003) Are high ³He/⁴He ratios in oceanic basalts an indicator of deep-mantle plume components ?
1017 *Earth Planet. Sci. Lett.* **208**, 197-204.
- 1018 Moreira M., Kunz J. and Allègre C. (1998) Rare gas systematics in popping rock: isotopic and
1019 elemental compositions in the upper mantle. *Science* **279**, 1178-1181.
- 1020 Moreira M. and Sarda P. (2000) Noble gas constraints on degassing process. *Earth and Planet. Sci.*
1021 *Lett.* **176**, 375-386.
- 1022 Namiki A. and Manga M. (2008) Transition between fragmentation and permeable outgassing of low
1023 viscosity magmas. *J. Volcanol. Geotherm. Res.* **169**, 48-60.
- 1024 Navon O., Chekmir A. and Lyakhovsky V. (1998) Bubble growth in highly viscous melts: theory,
1025 experiments, and autoexplosivity of dome lavas. *Earth Planet Sci. Lett.* **160**, 763-776.
- 1026 Pan V., Holloway J.R. and Hervig R.L. (1991) The pressure and temperature dependence of carbon
1027 dioxide solubility in tholeiitic basalt melts. *Geochim. Cosmochim. Acta* **55**, 1587-1595.

- 1028 Paonita A. and Martelli M. (2006) Magma dynamics at mid-ocean ridges by noble gas kinetic
1029 fractionation: Assessment of magmatic ascent rates. *Earth Planet. Sci. Lett.* **241**, 138-158.
- 1030 Paonita A. and Martelli M. (2007) A new view of the He-Ar-CO₂ degassing at mid-ocean ridges:
1031 Homogeneous composition of magmas from the upper mantle. *Geochim. Cosmochim. Acta* **71**, 1747-
1032 1763.
- 1033 Parman S.W., Kurz M.D., Hart S.R. and Grove T.L. (2005) Helium solubility in olivine and
1034 implications for high ³He/⁴He in ocean island basalts. *Nature* **437**, 1140-1143.
- 1035 Pepin R.O. (2006) Atmospheres on the terrestrial planets: Clues to origin and evolution. *Earth Planet.*
1036 *Sci. Lett.* **252**, 1-14.
- 1037 Pineau F., Shilobreeva S., Hékinian, Bideau D. and Javoy M (2004) Deep sea activity on the Mid-
1038 Atlantic Ridge near 34°50'N: a stable isotope (C, H, O) study. *Chem. Geol.* **211**, 159-175.
- 1039 Porcelli D. and Wasserburg G.J. (1995) Mass transfer of helium, neon, argon, and xenon through a
1040 steady-state upper mantle. *Geochim. Cosmochim. Acta* **59**, 4921-4937.
- 1041 Prousevitch A.A., Sahagian D.L. and Anderson A.T. (1993) Dynamics of diffusive bubble growth in
1042 magmas: Isothermal case. *J. Geophys. Res.* **98**, 22,283-22,307.
- 1043 Prousevitch A.A. and Sahagian D.L (1998) Dynamics and energetics of bubble growth in magmas:
1044 Analytical formulation and numerical modeling. *J. Geophys. Res.* **103**, 18,223-18,251.
- 1045 Raquin A., Moreira M.A. and Guillon F. (2008) He, Ne, Ar systematics in single vesicles: Mantle
1046 isotopic ratios and origin of the air component in basaltic glasses. *Earth Planet Sci. Lett.* **274**, 142-
1047 150.
- 1048 Rooney T.O., Herzberg C. and Bastow I.D. (2012) Elevated mantle temperature beneath East Africa.
1049 *Geology* **40**, 27-30.
- 1050 Ryan M.P. and Sammis C.G. (1981) The glass transition in basalt. *J. Geophys. Res.* **86**, 9519-9535.
- 1051 Saal A.E., Hauri E.H., Langmuir C.H. and Perfit M.R. (2002) Vapour undersaturation in primitive
1052 mid-ocean-ridge basalt and the volatile content of Earth's upper mantle. *Nature* **419**, 451-455.
- 1053 Sarda P. and Guillot B. (2005) Breaking of Henry's law for noble gas and CO₂ solubility in silicate
1054 melt under pressure. *Nature* **436**, 95-98.
- 1055 Sarda P. and Graham D. (1990) Mid-ocean ridge popping rocks: implications for degassing at ridge
1056 crests. *Earth Planet. Sci. Lett.* **97**, 268-289.

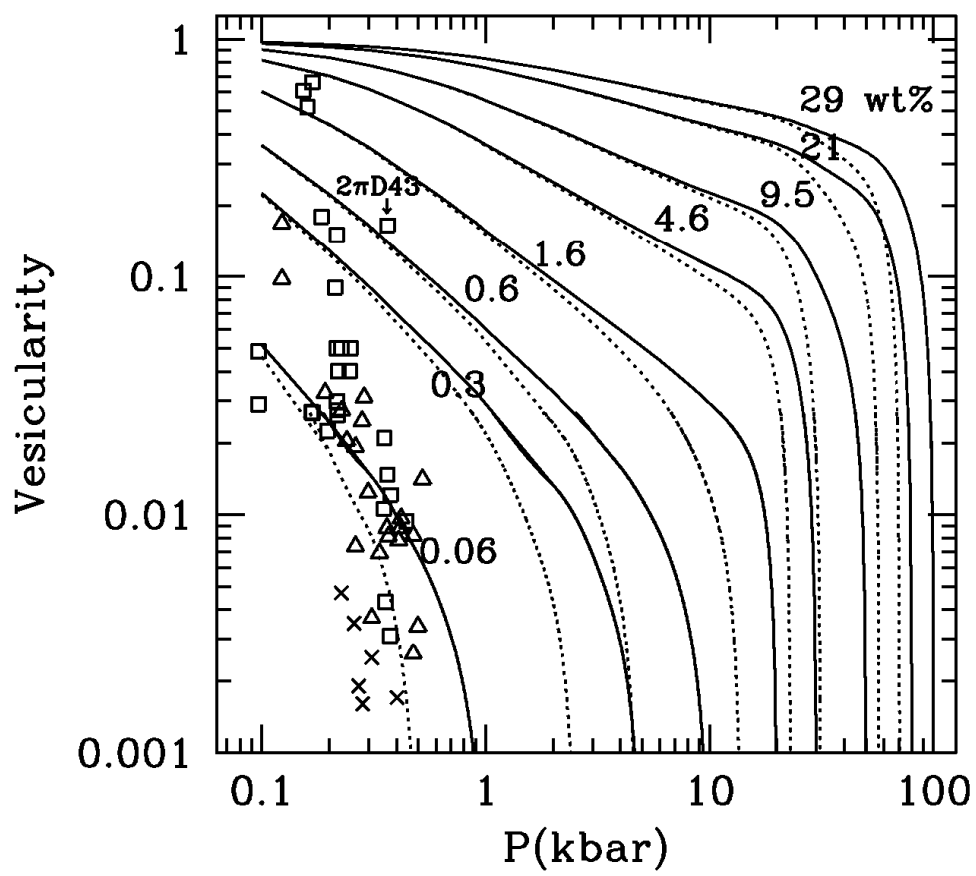
- 1057 Sarda P. and Moreira M. (2002) Vesiculation and vesicle loss in mid-ocean ridge basalt glasses: He,
1058 Ne, Ar elemental fractionation and pressure influence. *Geochim. Cosmochim. Acta* **66**, 1449-1458.
- 1059 Sasinovskii V (1979) *Trudy Moskovskogo Energeticheskogo Instituta* **364**, 13-18.
- 1060 Shaw A.M., Behn M.D., Humphris S. E., Sohn R. A. and Gregg P.M. (2010) Deep pooling of low
1061 degree melts and volatile fluxes at the 85°E segment of the Gakkel Ridge: Evidence from olivine-
1062 hosted melt inclusions and glasses. *Earth Planet. Sci. Lett.* **289**, 311-322.
- 1063 Shing K.S., Gubbins K.E. and Lucas K. (1988) Henry constants in non-ideal fluid mixtures: computer
1064 simulation and theory. *Mol. Phys.* **65**, 1235-1252.
- 1065 Smith W. and Forester T. (1996) DL_POLY_2.0: a general-purpose parallel molecular dynamics
1066 simulation package. *J. Mol. Graph.* **14**, 136-141.
- 1067 Sohn R.A., Willis C., Humphris S., Shank T.M., Singh H., Edmonds H.N., Kunz K., Hedman U.,
1068 Helmkr E., Jakuba M., Liljebladh B., Linder J., Murphy C., Nakamura K.-I, Sato T., Schindwein V.,
1069 Stranne C., Tausenfrennd M., Upchurch L., Winsor P., Jakobsson M and Soule A.(2008) Explosive
1070 volcanism on the ultralow-spreading Gakkel ridge, Arctic Ocean. *Nature* **453**, 1236-1238.
- 1071 Sparks R.S.J. (1978) The dynamics of bubble formation and growth in magmas: A review and
1072 analysis. *J. Volcanol. Geotherm. Res.* **3**, 1-37.
- 1073 Stolper E. and Holloway J.R. (1988) Experimental determination of the solubility of carbon dioxide in
1074 molten basalt at low pressure. *Earth Planet. Sci. Lett.* **87**, 397-408.
- 1075 Thomsen T.B. and Schmidt M.W. (2008) Melting of carbonated pelites at 2.5-5.0 GPa, silicate-
1076 carbonatite liquid immiscibility, and potassium-carbon metasomatism of the mantle. *Earth Planet Sci.*
1077 *Lett.* **267**, 17-31.
- 1078 Toramaru A. (1995) Numerical study of nucleation and growth of bubbles in viscous magmas. *J.*
1079 *Geophys. Res.* **100**, 1913-1931.
- 1080 Vrabc J., Stoll J. and Hasse H. (2001) A set of models for symmetric quadrupolar fluids. *J. Phys.*
1081 *Chem. B* **105**, 12126-12133.
- 1082 Vrabc J., Huang Y.-L. and Hasse H. (2009) Molecular models for 267 binary mixtures validated by
1083 vapor-liquid equilibria: A systematic approach. *Fluid Phase Equilib.* **279**, 120-135.
- 1084 Walker D. and Mullins O. (1981) Surface tension of natural silicate melts from 1,200°-1,500°C and
1085 implications for melt structure. *Contrib. Mineral. Petrol.* **76**, 455-462.

- 1086 Widom B. (1963) Some topics in theory of fluids. *J. Chem. Phys.* **39**, 2808-2812.
- 1087 Yamamoto J., Nishimura K., Sugimoto T., Takemura K., Takahata N. and Sano Y. (2009) Diffusive
1088 fractionation of noble gases in mantle with magma channels: Origin of low He/Ar in mantle-derived
1089 rocks. *Earth Planet. Sci. Lett.* **280**, 167-174.
- 1090 Zeng G., Chen L.-H., Xu X.-S., Jiang S.-Y. and Hofmann A.W. (2010) Carbonated mantle sources for
1091 Cenozoic intra-plate alkaline basalts in Shandong, North China. *Chem. Geol.* **273**, 35-45.
- 1092 Zhang Z. and Duan Z. (2005) An optimized molecular potential for carbon dioxide. *J. Chem. Phys.*
1093 **122**, 214507-1-15.
- 1094
- 1095
- 1096
- 1097
- 1098
- 1099
- 1100
- 1101
- 1102
- 1103
- 1104
- 1105
- 1106
- 1107
- 1108
- 1109
- 1110

1111

1112

1113



1114

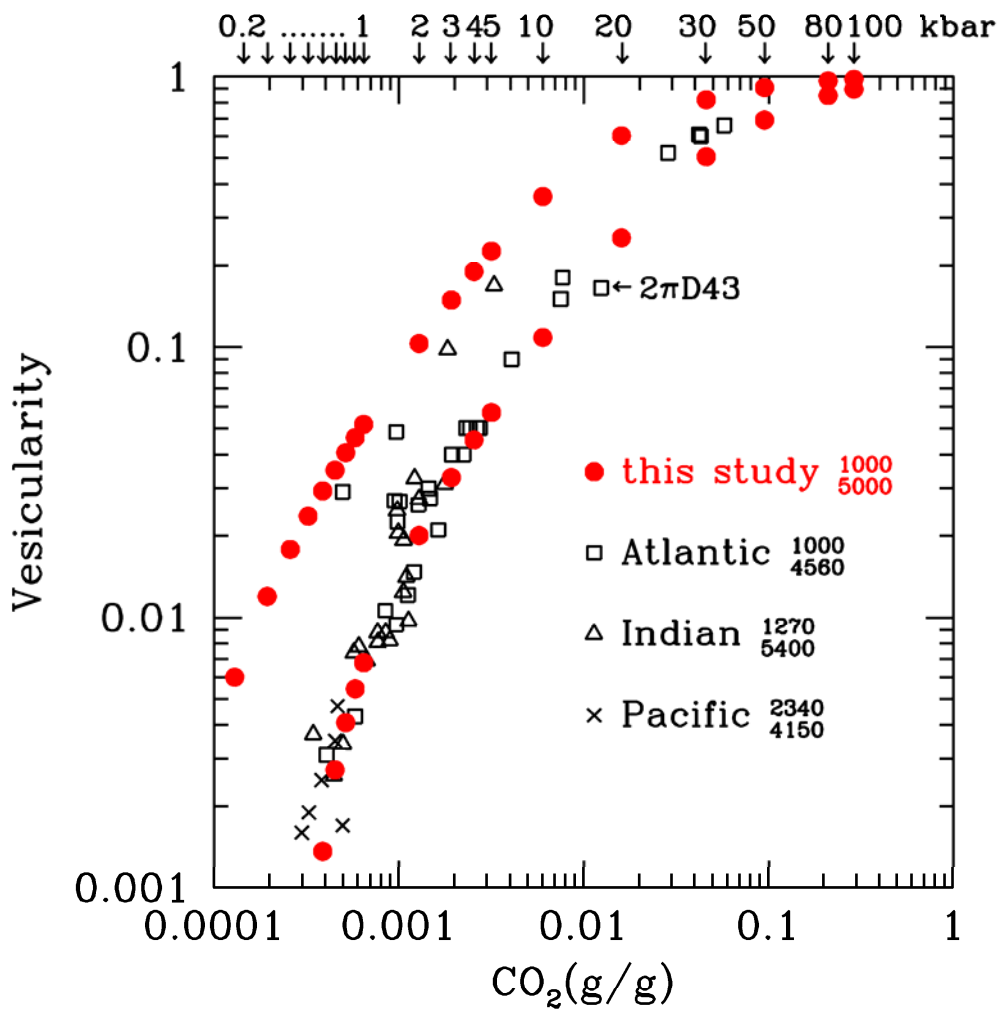
1115

1116

1117

1118

Fig.1



1119

1120

Fig.2

1121

1122

1123

1124

1125

1126

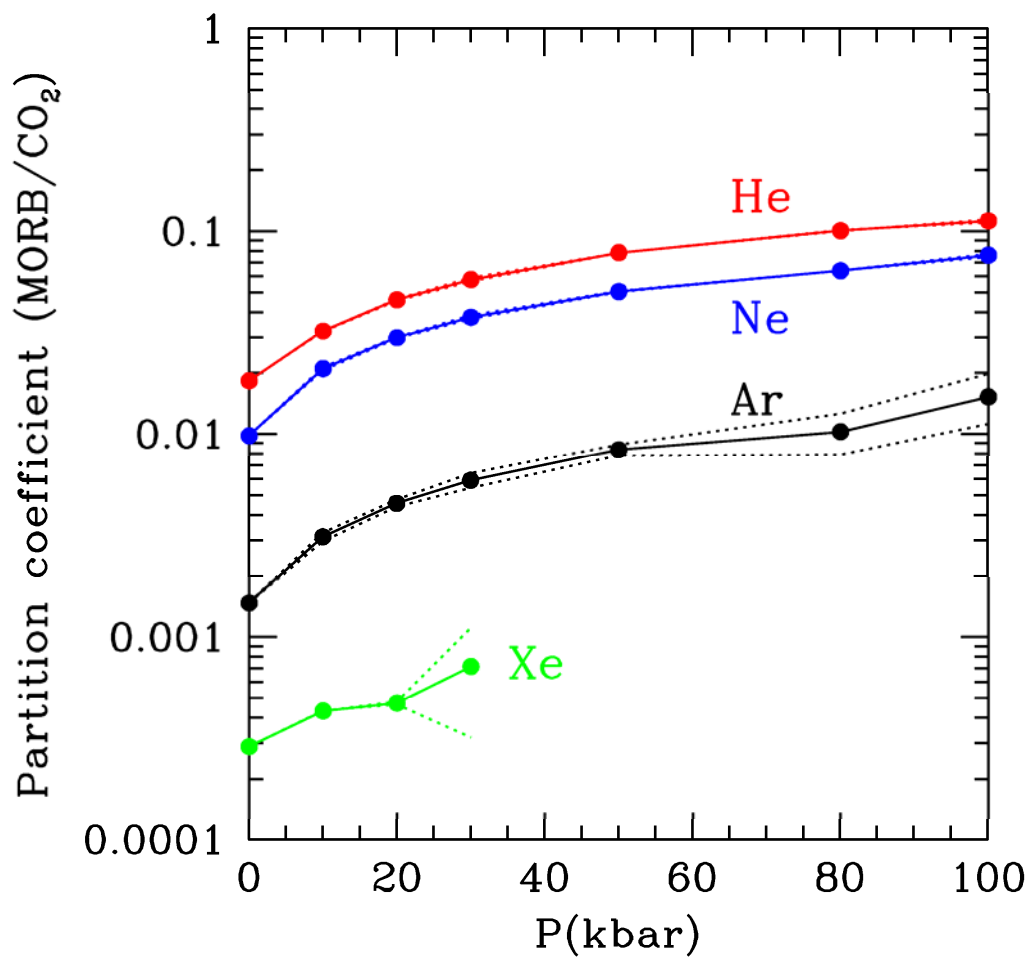


Fig.3

1127

1128

1129

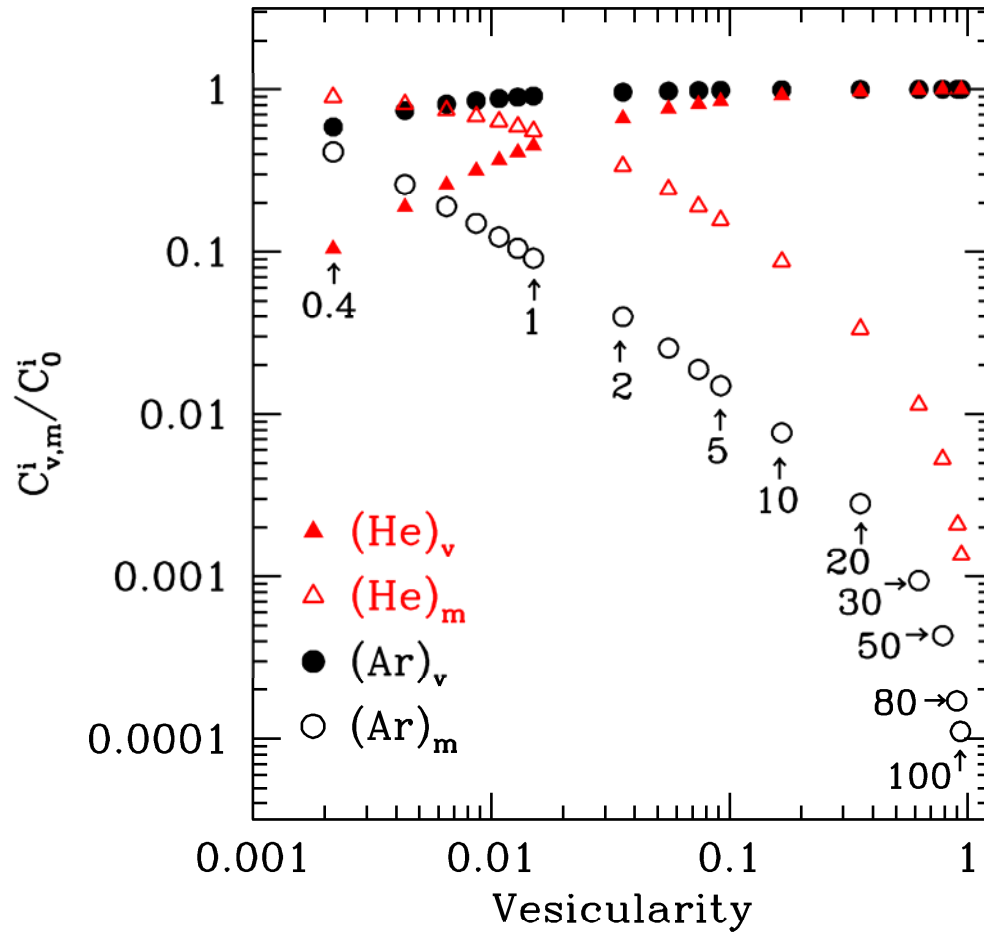
1130

1131

1132

1133

1134



1135

1136

1137

1138

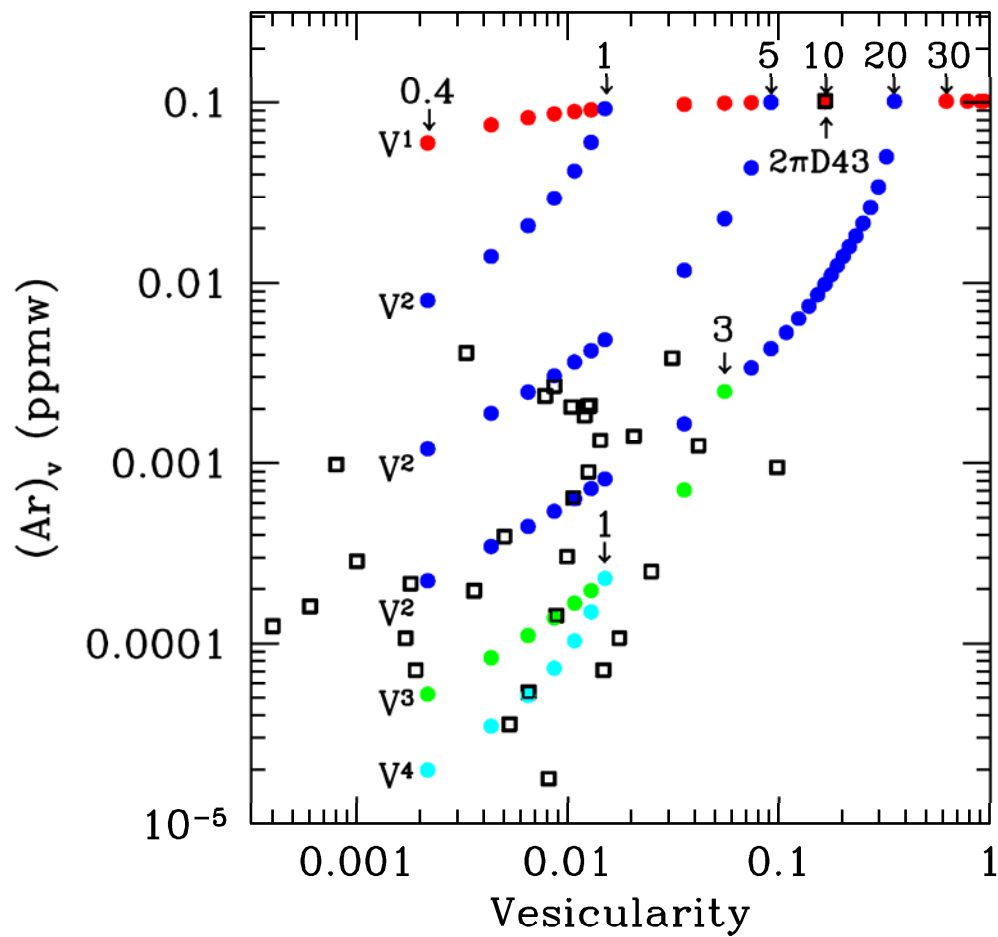
1139

1140

1141

1142

Fig.4



1143

1144

Fig.5

1145

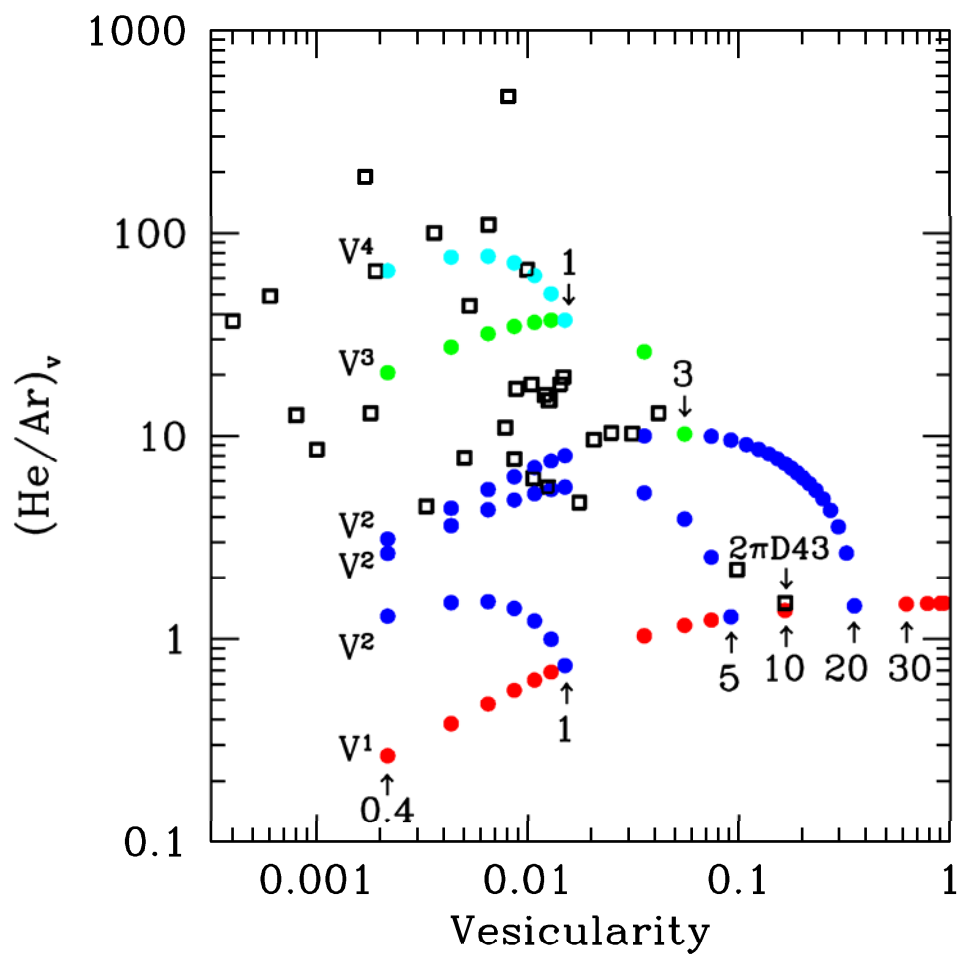
1146

1147

1148

1149

1150



1151

1152

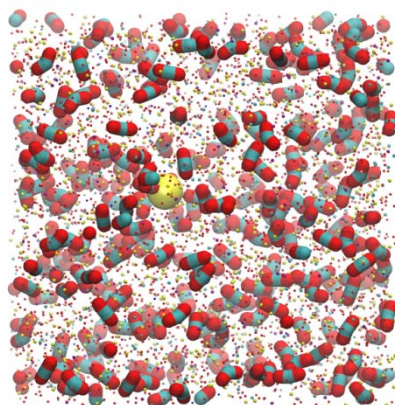
Fig.6

1153

1154

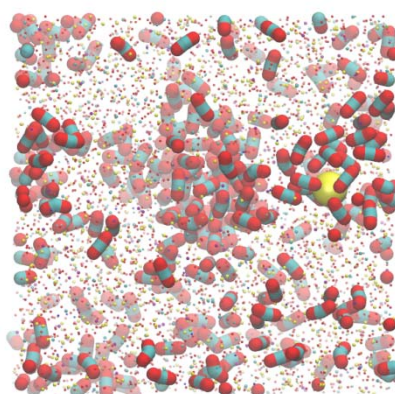
1155

1156



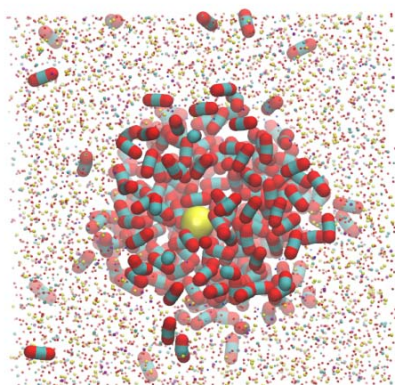
1157

(a)



1158

(b)



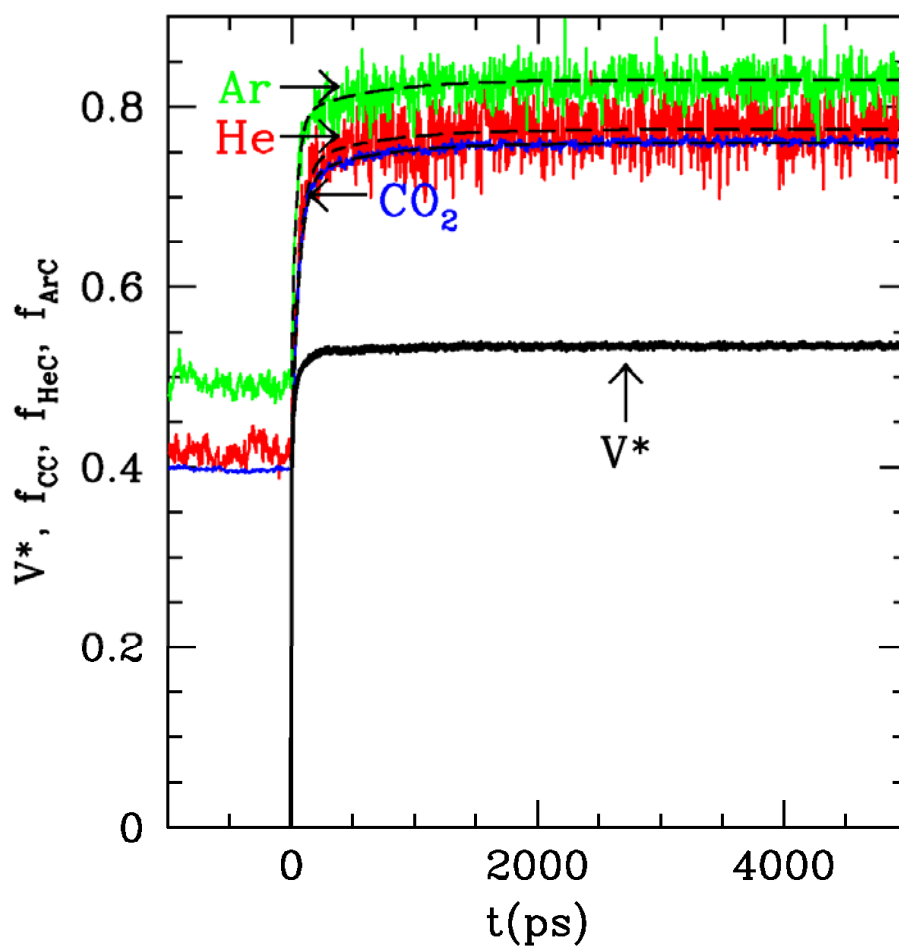
1159

(c)

Fig.7

1160

1161



1162

1163

1164

1165

1166

Fig.8